specificity (i.e., binding of the probe to a perfectly matched sequence rather than to regions with sequence mismatches).

Seven primer/probe sets were designed for this study. Fig. 1 shows a schematic diagram of the strategy for mutation detection using these primer/probe sets. Tables 1 and 2 list the primer/probe sets and corresponding sequences and primer concentrations that were used to target the 11 mutations. Primer/probe sets A, B, C, D, E, and F were designed to detect mutations [I], [II], [III], [IV], [V], and [XIX], respectively. Primer/probe set G was designed to detect the five mutations clustered on exon 17: mutations [VI], [VII], [VIII], [IX], and [XXI] (Fig. 1D). All primers and probes were synthesized based on the NCBI reference SLC25A13 gene sequence (GenBank accession no. **NM_014251**) with the exception of mutation [XIX]:IVS16ins3kb, which was designed according to [19].

Real-time PCR and subsequent melting curve analyses were performed in a closed tube using a 20-μL mixture on a LightCycler 1.5 (Roche Diagnostics, Tokyo, Japan). The PCR mixture contained 2.0 μL of genomic DNA (10–50 ng), 0.5 μM of forward primer, 0.5 or 0.1 μM of reverse primer, 0.2 μM of each sensor and anchor probe, and 10 μL of Premix ExTaq™ (Perfect Real Time) reagent (TaKaRa Bio Inc., Otsu, Japan).

The thermal profile conditions were identical for all seven assays and consisted of an initial denaturation step (30 s at 95 °C), followed by 45 amplification cycles with the following conditions: denaturation for 5 s at 95 °C and annealing and extension for 20 s at 60 °C. The transition rate between all steps was 20 °C/s. After amplification, the samples were held at 37 °C for 1 min, followed by the melting curve acquisition at a ramp rate of 0.15 °C/s extending to 80 °C with continuous fluorescence acquisition.

Table 2
Primers, probes and target amplicon sequences, target mutation sites, and primer concentrations.

Primer/probe set	Name	Sequences of PCR products, primer locations, probe sequences, and mutation sites (5′ to 3′)	Concentration (μmol/L)
A		GGCTATACTGAAATATGAGAAatgaaaaaagggatgtttttaaatttataatgtaaattgtaataaattggtatatttgttgcttgtgtttgtttttcccctacagac	
		gtatgaccttagcagacattgaacggattgctcctctggaagagggaactctgccCTTTAACTTGGCTGAGG (181 bp)	
	Mut1-F	GGCTATACTGAAATATGAGAA	0.5
	Mut1-R	CCTCAGCCAAGTTAAAG	0.5
	Mut1-UP	ATGTAAATTGTAATAAATTGGTATATTTGTTGCTTGTGTT-FITC	
	Mut1-DW	LC Red640-GTTTTTCCCCTACAGAC**GACC**-P	
B		GAATGCAGAACCAACGAtcaactggctcttttgtgggagaactcatgtataaaaacagctttgactgttttaagaaagtgctacgctatgaaggcttctt	
		tggactgtatagag**g**ttagtgccacatgctcaatacctgttaggtgaaataacactcaaaggtttggtttctcatcttagtgcctGACATGAATTAGCAAGACTG (205 bp)	
	Mut2-F	GAATGCAGAACCAACGA	0.5
	Mut2-R	CAGTCTTGCTAATTCATGTC	0.1
	Mut2-UP	ACCTAACAGGTATTGAGCATGTG-FITC	
	MUt2-DW	LC Red640-CACTAA**C**CTCTATACAGTCCA-P	
C		GCAGTTCAAAGCACAGTTATTtttatatagtgagaatgtgaccagactgagatggtgttgtgtctctcctgcaggtatgcctgcagcatctttagtg	
		acccctgctgatgttatcaagacgagattacaggtg	
		gctgcccggg(**gagatta**caggtggctgcccggg)ctggccaaaccaCTTACAGCGGAGTGATAGAC (175 bp)	
	Mut3-F	GCAGTTCAAAGCACAGTTATT	0.5
	Mut3-R	GTCTATCACTCCGCTGTAAG	0.5
	Mut3-UP	ACCCCTGCTGATGTTATCAAGACGAGATTACAGGT-FITC	
	Mut3-DW	LC Red640-GCTGCCCGGG**GAGATTA**-P	
D		TCAATTTATTTGAGGCTGCtggaggtaccacatcccatcaagttagtttctcctattttaatggatttaatt**c**gctcctt**a**acaac	
		atggaactcattagaaagatctatagcactc	
		tggctggcaccaggaaagatgttgaagtGACTAAGGGTGAGTGAGAA (164 bp)	
	Mut4-F	TCAATTTATTTGAGGCTGC	0.5
	Mut4-R	TTCTCACTCACCCTTAGTC	0.5
	Mut4-UP	AATGGATTTAATT**C**GCTCCTTAACA-FITC	
	Mut4-DW	LC Red640-ATGGAACTCATTAGAAAGATCTATAGCACTC-P	
E		TGCACAAAGATGGTTCGgtcccacttgcagcagaaattcttgctggaggctg**c**gtaagtacctttt**g**aagctctcttcattgaaaagacttgtttcac	
		atatatatcactaccatggtcaacaggtgtggactaaggcttctgttTAACCACAGATCCTGCA (162 bp)	
	Mut5-F	TGCACAAAGATGGTTCG	0.5
	Mut5-R	TGCAGGATCTGTGGTTA	0.5
	Mut5-UP	GTGAAACAAGTCTTTTCAATGAAGAGAGCTTC-FITC	
	Mut5-DW	LC Red640-AAGGTACTTA**C**GCAGCCTC-P	
F	normal allele	GGAGCTGGTGGTATGGAAataatgtgttcttaactaactctttggtatcaggtaaatttttaaaatatctaattatatctgtgatttctc	
		catttttttaaagctcgtgtatttcgatcctcaccccagtttggt	
		gtaactttgctgacttacgaattgctacagcgatggttctacattgattttggaggagtgtaagtatcatgctaaatctgctgctaaatttt	
		GGCTGCTGCTAATGCTC (244 bp)	
	insertion allele	CCATCTTCCTCCTCCCTTggcagccccgccccccgatttctccatttttttaaagctcgtgtatttcgatcctcaccccagtttggt	
		gtaactttgctgacttacgaattgctacagcgatggttctacattgatttt	
		ggaggagtgtaagtatcatgctaaatctgctgctaaattttGGCTGCTGCTAATGCTC (196 bp)	
	Mut19-N-F	GGAGCTGGTGGTATGGAA	0.5
	Mut19-ins-F	CCATCTTCCTCCTCCCTT	0.5
	Mut19-R	GAGCATTAGCAGCAGCC	0.5
	Mut19-UP	ACCAAACTGGGGTGAGGATCGAAATACACGAGCTTTAAAAAAATG-FITC	
	Mut19-N-DW	LC Red640-AGAAATCACAGATATAATTAGATATTT-P	
	Mut19-ins-DW	LC Red640-AGAAATCGGGGGGCGGGG-P	
G		TCTTAACTAACTCTTTGGTATCAGGTaaatttttaaaatatctaattatatctgtgatttctccatttttttaaagctcg	
		tgtatttcgatcctcaccccagtttggtgtaactttg**c**t**g**actt**a(a)cg**aattgctacag**c**ga	
		tggttctacattgattttggaggagtgtaagtatcatgctaaatctgctgctaaattttGGCTGCTGCTAATGCTC (217 bp)	
	Mut6-9, 21-F	TCTTAACTAACTCTTTGGTATCAGGT	0.5
	Mut6-9, 21-R	GAGCATTAGCAGCAGCC	0.5
	Mut6-9, 21-UP	TGTATTTCGATCCTCACCCCAGTTTGGTGTAACTT-FITC	
	Mut6-9, 21-DW	LC Red640-GC**G**GACTT**ACG**AATTGCTACAG**C**GA-P	

Upper case and underlined letters indicate the locations of primers and probes, respectively. Inserted DNA is shown in parenthesis. Nucleotides in boldface were used for mutation detection.
F: forward, R: reverse, UP: upstream, DW: downstream, N: normal allele, ins: insertion allele, FITC: fluorescein isothiocyanate, P: phosphate.

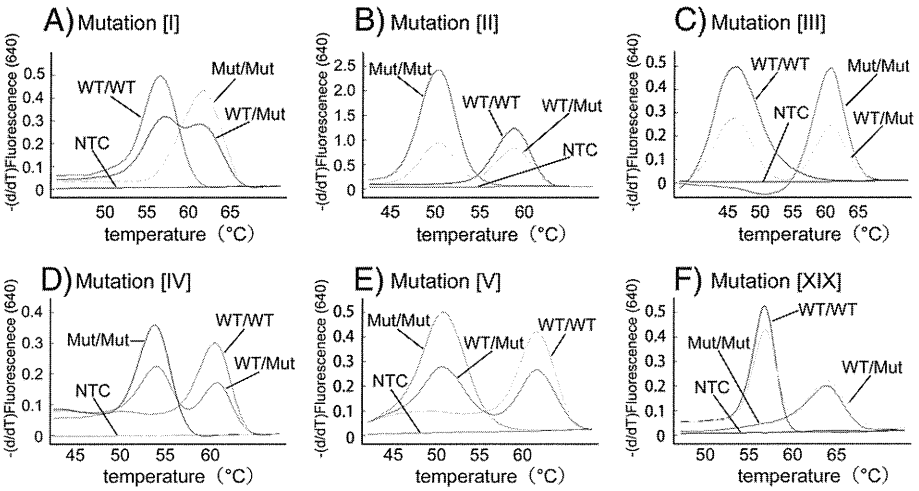

Fig. 2. Typical melting curves used in the detection of mutations [I–V] and [XIX]. Each assay using primer/probe sets A–F is displayed in a separate graph (A–F). WT: wild-type allele, Mut: mutant allele, NTC: no DNA template control.

2.3. Validation of the mutation detection system

After establishing the protocol for detecting the 11 prevalent mutations, 50 DNA samples from patients' blood were sent from Kagoshima University to Tohoku University for the validation of this system in a single-blind manner. Similarly, 26 DNA samples purified from paper-filter blood samples were analyzed in the same manner as the blood DNA samples.

2.4. Estimation of the carrier frequency

For the estimation of the heterozygous carrier frequency, 420 genomic DNA samples from healthy volunteers were screened using the HybProbe analysis for the 11 prevalent mutations. All detected mutations were confirmed by direct sequencing.

2.5. Ethics

This study was approved by the Ethical Committees of Tohoku University School of Medicine and Kagoshima University. Written informed consent was obtained from all participants or their guardians.

3. Results

3.1. Development of the mutation detection system

In primer/probe sets B, D, and E, the reporter probes were designed to be complimentary to the wild-type allele (Fig. 1A). To allow for an improved detection of the mutations, primer/probe sets A and C were designed to be complementary to the mutant allele (Figs. 1B, C). In the primer/probe set F, two forward PCR primers, which were specific to the wild-type and the mutant alleles, were used with a common reverse primer for the co-amplification of the wild-type and 3-kb insertion alleles (Fig. 1E). Two reporter probes, which had a common anchor probe, were used for the detection of the wild-type and mutant alleles. Because the two reporter probes had different melting temperatures, we were able to identify the allele that was amplified. Fig. 2 shows representative results of the melting curve analyses using the primer/probe sets A–F, in which all of the mutant alleles generated distinct peaks corresponding to the wild-type alleles.

In the primer/probe set G, we used a reporter probe that was complementary to the mutant [XXI] allele (Fig. 1D). All five mutations in exon 17 were successfully differentiated from the wild-type allele (Figs. 3A–E). The [XXIX] mutation is an additional mutation in exon

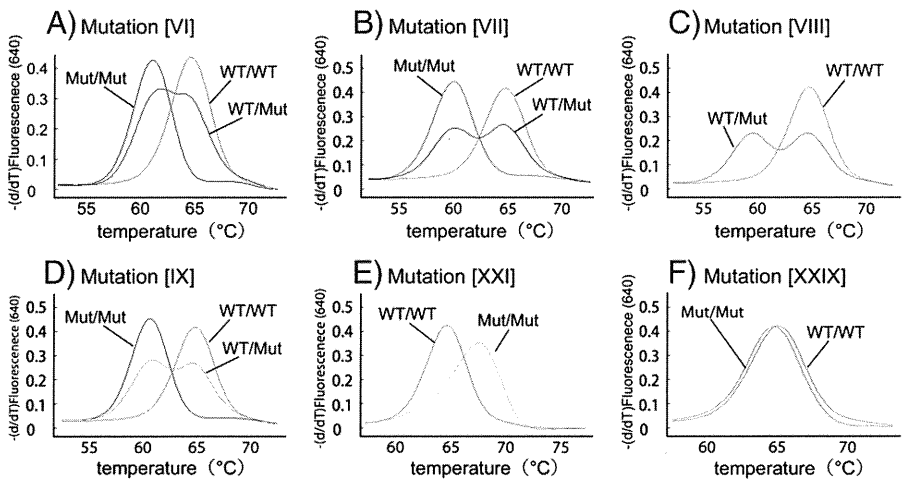

Fig. 3. Typical melting curves used in the detection of mutations [VI–XI], [XXI], and [XXIX] on exon 17. Genotyping was performed using primer/probe set G. Each melting curve for a target mutation is displayed in a separate graph (A–F). Note that mutation [XXIX] (F) is a non-target mutation on the anchor probe. WT: wild-type allele, Mut: mutant allele.

17 that is not listed in Table 1. The [XXIX] mutation is located in the anchor-probe binding site and not on the reporter-probe binding site (Fig. 1D). To examine the effect of mutations on the anchor probe, we genotyped a patient with a heterozygous [XXIX] mutation using primer/probe set G (Fig. 3F). We found no change in the melting curves between the wild-type allele and the [XXIX] allele, thereby suggesting that point mutations within the anchor probe sequence have little effect on the melting curve analysis.

3.2. Validation

The genotypes determined at Tohoku University using the proposed method and those determined at Kagoshima University using a previously published method were identical for the 11 common mutations (Table S1 in supplementary material). We performed a similar test using DNA samples purified from filter-paper blood samples to determine if this method could be used for newborn screening. The genotypes determined in both laboratories were identical for all 26 DNA samples (Table S2 in supplementary material).

3.3. Frequency of eleven prevalent mutations

We found four heterozygous carriers of mutation [I], three of mutation [II], and two of mutation [V]. In addition, primer/probe set G detected one heterozygous mutation, which was confirmed as mutation [VIII] by direct sequencing. Altogether, 10 mutations were detected in 420 Japanese healthy controls.

4. Discussion

We developed a simple and rapid genetic test using real-time PCR combined with the HybProbe system for the 11 prevalent mutations in *SLC25A13*: mutations [I], [II], [III], [IV], [V], [VI], [VII], [VIII], [IX], [XIX], and [XXI]. This genetic test is a closed-tube assay in which no post-PCR handling of the samples is required. In addition, the genotyping is completed within 1 h. This test can utilize DNA samples purified from both peripheral blood and filter-paper blood. The reliability of the test was confirmed by genotyping 76 blind DNA samples from patients with citrin deficiency, including 50 peripheral blood and 26 filter-paper blood DNA samples. Because screening for the 11 targeted mutations would identify 95% of mutant alleles in the Japanese population [19], both, one, and no mutant alleles are expected to be identified in 90.4%, 9.3%, and less than 0.3% of patients, respectively. This genetic test would be useful not only in Japan but also other East Asian countries, including China, Korea, Taiwan and Vietnam, in which the same mutations are prevalent. Our test is expected to detect 76–87% of the mutant alleles in the Chinese population [12,19,25], 95–100% in the Korean population [12,19,26], 60–68% in the Taiwanese population [27,28], and 100% in the Vietnamese population [12,19]. If we were to prepare a primer/probe set for mutation [X]:g.IVS6+5G>A [12], which is prevalent in Taiwan, the estimated sensitivity would exceed 90% in the Taiwanese population [27,28].

Recently, the high resolution melting (HRM) method was reported to be suitable for the screening of mutations in the diagnosis of citrin deficiency [28]. HRM analysis is a closed-tube assay that screens for any base changes in the amplicons. The presence of SNPs anywhere on the amplicons can affect the melting curve, thereby suggesting that HRM is not suitable for screening for known mutations, but rather, is best suited to screening for unknown mutations. When we detected one heterozygous prevalent mutation, we performed HRM screening for all 17 exons of *SLC25A13*. After HRM screening, only the HRM-positive exons were subjected to direct sequencing analysis. Several mutant alleles were identified using this approach.

The frequency of homozygotes, including compound heterozygotes, presenting *SLC25A13* mutations in the population at Kagoshima (a prefecture in the southern part of Japan) has been calculated to be 1/17,000 based on the carrier rate (1/65) [19]. The prevalence of NICCD has been also reported to be 1/17,000–34,000 [29]. In this study, the carrier rate in Miyagi (a prefecture in northern Japan) was 1/42 (95% confidential interval, 1/108–1/26), thereby yielding an estimated frequency of patients with citrin deficiency of 1/7,100. Our result, together with the previous report [19], suggests that a substantial fraction of the homozygotes or compound heterozygotes of SLC25A13 mutations was asymptomatic during the neonatal period.

The early and definitive diagnosis of citrin deficiency may be beneficial for patients with citrin deficiency by encouraging specific dietary habits and avoiding iatrogenic worsening of brain edema by glycerol infusion when patients develop encephalopathy [30,31]. Because the screening of blood citrulline levels by tandem mass analysis at birth does not detect all patients with citrin deficiency, the development of a genetic test would be welcomed. In this study, we demonstrated that genomic DNA extracted from filter paper blood samples was correctly genotyped, thereby indicating the feasibility of newborn screening using this genetic test. If 100,000 babies in the northern part of Japan were screened by this method, we would detect 14 homozygotes or compound heterozygotes with *SLC25A13* mutations and 2400 heterozygous carriers. In 2400 heterozygous carriers, we would expect to observe only 1 to 2 compound heterozygotes with one target and one non-target mutation. The estimated frequency of babies with two non-target mutations is 0.04/100,000. Our genetic method would therefore allow us to screen newborn babies efficiently. If we performed this genetic test in a high-throughput real-time PCR system, such as a 384- or 1,536-well format, the cost per sample could be lowered.

In conclusion, we have established a rapid and simple detection system using the HybProbe assay for the 11 prevalent mutations in *SLC25A13*. This system could be used to screen newborns for citrin deficiency and may facilitate the genetic diagnosis of citrin deficiency, especially in East Asian populations.

Supplementary materials related to this article can be found online at doi:10.1016/j.ymgme.2011.12.024.

Acknowledgments

The authors acknowledge the contribution of Dr. Keiko Kobayashi, who passed away on December 21th, 2010. Dr. Kobayashi discovered that the *SLC25A13* gene is responsible for citrin deficiency and devoted much of her life to elucidating the mechanism of citrin deficiency. This work was supported by grants from the Ministry of Education, Culture, Sports, Science, and Technology and the Ministry of Health, Labor, and Public Welfare.

References

[1] K. Kobayashi, D.S. Sinasac, M. Iijima, A.P. Boright, L. Begum, J.R. Lee, T. Yasuda, S. Ikeda, R. Hirano, H. Terazono, M.A. Crackower, I. Kondo, L.C. Tsui, S.W. Scherer, T. Saheki, The gene mutated in adult-onset type II citrullinaemia encodes a putative mitochondrial carrier protein, Nat. Genet. 22 (1999) 159–163.
[2] T. Ohura, K. Kobayashi, Y. Tazawa, I. Nishi, D. Abukawa, O. Sakamoto, K. Iinuma, T. Saheki, Neonatal presentation of adult-onset type II citrullinemia, Hum. Genet. 108 (2001) 87–90.
[3] Y. Tazawa, K. Kobayashi, T. Ohura, D. Abukawa, F. Nishinomiya, Y. Hosoda, M. Yamashita, I. Nagata, Y. Kono, T. Yasuda, N. Yamaguchi, T. Saheki, Infantile cholestatic jaundice associated with adult-onset type II citrullinemia, J. Pediatr. 138 (2001) 735–740.
[4] T. Tomomasa, K. Kobayashi, H. Kaneko, H. Shimura, T. Fukusato, M. Tabata, Y. Inoue, S. Ohwada, M. Kasahara, Y. Morishita, M. Kimura, T. Saheki, A. Morikawa, Possible clinical and histologic manifestations of adult-onset type II citrullinemia in early infancy, J. Pediatr. 138 (2001) 741–743.
[5] T. Shigeta, M. Kasahara, T. Kimura, A. Fukuda, K. Sasaki, K. Arai, A. Nakagawa, S. Nakagawa, K. Kobayashi, S. Soneda, H. Kitagawa, Liver transplantation for an

infant with neonatal intrahepatic cholestasis caused by citrin deficiency using heterozygote living donor, Pediatr. Transplant. 14 (2009) E86–88.
[6] M. Kasahara, S. Ohwada, T. Takeichi, H. Kaneko, T. Tomomasa, A. Morikawa, K. Yonemura, K. Asonuma, K. Tanaka, K. Kobayashi, T. Saheki, I. Takeyoshi, Y. Morishita, Living-related liver transplantation for type II citrullinemia using a graft from heterozygote donor, Transplantation 71 (2001) 157–159.
[7] Y. Takashima, M. Koide, H. Fukunaga, M. Iwai, M. Miura, R. Yoneda, T. Fukuda, K. Kobayashi, T. Saheki, Recovery from marked altered consciousness in a patient with adult-onset type II citrullinemia diagnosed by DNA analysis and treated with a living related partial liver transplantation, Intern. Med. 41 (2002) 555–560.
[8] A. Tamamori, Y. Okano, H. Ozaki, A. Fujimoto, M. Kajiwara, K. Fukuda, K. Kobayashi, T. Saheki, Y. Tagami, T. Yamano, Neonatal intrahepatic cholestasis caused by citrin deficiency: severe hepatic dysfunction in an infant requiring liver transplantation, Eur. J. Pediatr. 161 (2002) 609–613.
[9] T. Ohura, K. Kobayashi, Y. Tazawa, D. Abukawa, O. Sakamoto, S. Tsuchiya, T. Saheki, Clinical pictures of 75 patients with neonatal intrahepatic cholestasis caused by citrin deficiency (NICCD), J. Inherit. Metab. Dis. 30 (2007) 139–144.
[10] T. Yasuda, N. Yamaguchi, K. Kobayashi, I. Nishi, H. Horinouchi, M.A. Jalil, M.X. Li, M. Ushikai, M. Iijima, I. Kondo, T. Saheki, Identification of two novel mutations in the SLC25A13 gene and detection of seven mutations in 102 patients with adult-onset type II citrullinemia, Hum. Genet. 107 (2000) 537–545.
[11] N. Yamaguchi, K. Kobayashi, T. Yasuda, I. Nishi, M. Iijima, M. Nakagawa, M. Osame, I. Kondo, T. Saheki, Screening of SLC25A13 mutations in early and late onset patients with citrin deficiency and in the Japanese population: identification of two novel mutations and establishment of multiple DNA diagnosis methods for nine mutations, Hum. Mutat. 19 (2002) 122–130.
[12] Y.B. Lu, K. Kobayashi, M. Ushikai, A. Tabata, M. Iijima, M.X. Li, L. Lei, K. Kawabe, S. Taura, Y. Yang, T.-T. Liu, S.-H. Chiang, K.-J. Hsiao, Y.-L. Lau, L.-C. Tsui, D.H. Lee, T. Saheki, Frequency and distribution in East Asia of 12 mutations identified in the SLC25A13 gene of Japanese patients with citrin deficiency, J. Hum. Genet. 50 (2005) 338–346.
[13] E. Ben-Shalom, K. Kobayashi, A. Shaag, T. Yasuda, H.-Z. Gao, T. Saheki, C. Bachmann, O. Elpeleg, Infantile citrullinemia caused by citrin deficiency with increased dibasic amino acids, Mol. Genet. Metab. 77 (2002) 202–208.
[14] J. Takaya, K. Kobayashi, A. Ohashi, M. Ushikai, A. Tabata, S. Fujimoto, F. Yamato, T. Saheki, Y. Kobayashi, Variant clinical courses of 2 patients with neonatal intrahepatic cholestasis who have a novel mutation of SLC25A13, Metab. Clin. Exp. 54 (2005) 1615–1619.
[15] A. Luder, A. Tabata, M. Iijima, K. Kobayashi, H. Mandel, Citrullinaemia type 2 outside East Asia: Israeli experience, J. Inherit. Metab. Dis. 29 (2006) 59.
[16] T. Hutchin, M. Preece, K. Kobayashi, T. Saheki, R. Brown, D. Kelly, P. McKiernan, A. Green, U. Baumann, Neonatal intrahepatic cholestasis caused by citirn deficiency (NICCD) in a European patient, J. Inherit. Metab. Dis. 29 (2006) 112.
[17] J.-S. Sheng, M. Ushikai, M. Iijima, S. Packman, K. Weisiger, M. Martin, M. McCracken, T. Saheki, K. Kobayashi, Identification of a novel mutation in a Taiwanese patient with citrin deficiency, J. Inherit. Metab. Dis. 29 (2006) 163.
[18] J.M. Ko, G.-H. Kim, J.-H. Kim, J.Y. Kim, J.-H. Choi, M. Ushikai, T. Saheki, K. Kobayashi, H.-W. Yoo, Six cases of citrin deficiency in Korea, Int. J. Mol. Med. 20 (2007) 809–815.
[19] A. Tabata, J.-S. Sheng, M. Ushikai, Y.-Z. Song, H.-Z. Gao, Y.-B. Lu, F. Okumura, M. Iijima, K. Mutoh, S. Kishida, T. Saheki, K. Kobayashi, Identification of 13 novel mutations including a retrotransposal insertion in SLC25A13 gene and frequency of 30 mutations found in patients with citrin deficiency, J. Hum. Genet. 53 (2008) 534–545.
[20] P.S. Bernard, R.S. Ajioka, J.P. Kushner, C.T. Wittwer, Homogeneous multiplex genotyping of hemochromatosis mutations with fluorescent hybridization probes, Am. J. Pathol. 153 (1998) 1055–1061.
[21] C.N. Gundry, P.S. Bernard, M.G. Herrmann, G.H. Reed, C.T. Wittwer, Rapid F508del and F508C assay using fluorescent hybridization probes, Genet. Test. 3 (1999) 365–370.
[22] T. Saheki, K. Kobayashi, I. Inoue, Hereditary disorders of the urea cycle in man: biochemical and molecular approaches, Rev. Physiol. Biochem. Pharmacol. 108 (1987) 21–68.
[23] K. Kobayashi, M. Horiuchi, T. Saheki, Pancreatic secretory trypsin inhibitor as a diagnostic marker for adult-onset type II citrullinemia, Hepatology 25 (1997) 1160–1165.
[24] Y. Tazawa, K. Kobayashi, D. Abukawa, I. Nagata, S. Maisawa, R. Sumazaki, T. Iizuka, Y. Hosoda, M. Okamoto, J. Murakami, S. Kaji, A. Tabata, Y.B. Lu, O. Sakamoto, A. Matsui, S. Kanzaki, G. Takada, T. Saheki, K. Iinuma, T. Ohura, Clinical heterogeneity of neonatal intrahepatic cholestasis caused by citrin deficiency: case reports from 16 patients, Mol. Genet. Metab. 83 (2004) 213–219.
[25] H.Y. Fu, S.R. Zhang, X.H. Wang, T. Saheki, K. Kobayashi, J.S. Wang, The mutation spectrum of the SLC25A13 gene in Chinese infants with intrahepatic cholestasis and aminoacidemia, J. Gastroenterol. 46 (2011) 510–518.
[26] K. Kobayashi, Y.B. Lu, M.X. Li, I. Nishi, K.-J. Hsiao, K. Choeh, Y. Yang, W.-L. Hwu, J.K.V. Reichardt, F. Palmieri, Y. Okano, T. Saheki, Screening of nine SLC25A13 mutations: their frequency in patients with citrin deficiency and high carrier rates in Asian populations, Mol. Genet. Metab. 80 (2003) 356–359.
[27] T. Saheki, K. Kobayashi, M. Iijima, M. Horiuchi, L. Begum, M.A. Jalil, M.X. Li, Y.B. Lu, M. Ushikai, A. Tabata, M. Moriyama, K.-J. Hsiao, Y. Yang, Adult-onset type II citrullinemia and idiopathic neonatal hepatitis caused by citrin deficiency: involvement of the aspartate glutamate carrier for urea synthesis and maintenance of the urea cycle, Mol. Genet. Metab. 81 (Suppl 1) (2004) S20–S26.
[28] J.T. Lin, K.J. Hsiao, C.Y. Chen, C.C. Wu, S.J. Lin, Y.Y. Chou, S.C. Shiesh, High resolution melting analysis for the detection of SLC25A13 gene mutations in Taiwan, Clin. Chim. Acta 412 (2011) 460–465.
[29] Y. Shigematsu, S. Hirano, I. Hata, Y. Tanaka, M. Sudo, N. Sakura, T. Tajima, S. Yamaguchi, Newborn mass screening and selective screening using electrospray tandem mass spectrometry in Japan, J. Chromatogr. B Analyt. Technol. Biomed. Life Sci. 776 (2002) 39–48.
[30] M. Yazaki, Y.-i. Takei, K. Kobayashi, T. Saheki, S.-I. Ikeda, Risk of worsened encephalopathy after intravenous glycerol therapy in patients with adult-onset type II citrullinemia (CTLN2), Intern. Med. 44 (2005) 188–195.
[31] H. Takahashi, T. Kagawa, K. Kobayashi, H. Hirabayashi, M. Yui, L. Begum, T. Mine, S. Takagi, T. Saheki, Y. Shinohara, A case of adult-onset type II citrullinemia—deterioration of clinical course after infusion of hyperosmotic and high sugar solutions, Med. Sci. Monit. 12 (2006) CS13–CS15.

Journal of Cerebral Blood Flow & Metabolism (2012) 32, 306–317

www.jcbfm.com

Altered postnatal development of cortico–hippocampal neuronal electric activity in mice deficient for the mitochondrial aspartate–glutamate transporter

Marta Gómez-Galán[1], Julia Makarova[1], Irene Llorente-Folch[2], Takeyori Saheki[3], Beatriz Pardo[2], Jorgina Satrústegui[2] and Oscar Herreras[1]

[1]*Department of Systems Neuroscience, Cajal Institute—CSIC, Madrid, Spain;* [2]*Department of Molecular Biology, Centre for Molecular Biology Severo Ochoa UAM-CSIC, and CIBER for Rare Diseases (CIBERER), Autonomous University of Madrid, Madrid, Spain;* [3]*Institute for Health Sciences, Tokushima Bunri University, Yamashiro-cho, Tokushima, Japan*

The deficiency in the mitochondrial aspartate/glutamate transporter Aralar/AGC1 results in a loss of the malate-aspartate NADH shuttle in the brain neurons, hypomyelination, and additional defects in the brain metabolism. We studied the development of cortico/hippocampal local field potential (LFP) in Aralar/AGC1 knockout (KO) mice. Laminar profiles of LFP, evoked potentials, and unit activity were recorded under anesthesia in young (P15 to P22) Aralar-KO and control mice as well as control adults. While LFP power increased 3 to 7 times in both cortex and hippocampus of control animals during P15 to P22, the Aralar-KO specimens hardly progressed. The divergence was more pronounced in the CA3/hilus region. In parallel, spontaneous multiunit activity declined severely in KO mice. Postnatal growth of hippocampal-evoked potentials was delayed in KO mice, and indicated abnormal synaptic and spike electrogenesis and reduced output at P20 to P22. The lack of LFP development in KO mice was accompanied by the gradual appearance of epileptic activity in the CA3/hilus region that evolved to status epilepticus. Strikingly, CA3 bursts were poorly conducted to the CA1 field. We conclude that disturbed substrate supply to neuronal mitochondria impairs development of cortico–hippocampal LFPs. Aberrant neuronal electrogenesis and reduced neuron output may explain circuit dysfunction and phenotype deficiencies.
Journal of Cerebral Blood Flow & Metabolism (2012) **32,** 306–317; doi:10.1038/jcbfm.2011.129; published online 21 September 2011

Keywords: Aralar/AGC1; aspartate–glutamate mitochondrial carrier; electroencephalographic activity; local field potential; OmniBank

Introduction

During postnatal brain development, many processes come to a final mature condition within a perfectly orchestrated temporal succession of events, for which cellular machinery should be ready. It has already come out evident that alterations in neurodevelopment may lead to brain pathology. There is also evidence that early electrical activity in the brain is key for development and refinement of functional networks (Khazipov and Luhmann, 2006). Activity-dependent modulation of metabolic pathways may thus determine the correct development at an early stage. We here report on the postnatal alterations of brain electrical activity in mice deficient in Aralar/AGC1, a mitochondrial transporter of aspartate–glutamate present mainly in neurons (del Arco and Satrústegui, 1998; Ramos *et al*, 2003; Berkich *et al*, 2007; Xu *et al*, 2007) that is critically involved in neuroglial metabolic concert (Pardo *et al*, 2011).

While disruption of neuroglial metabolic coupling in adult brain leads to failure of ion homeostasis, neurotransmission, and cell survival (Largo *et al*, 1996), little is known in the early postnatal period,

Correspondence: Dr O Herreras, Department of Systems Neuroscience, Cajal Institute—CSIC, Avenue Doctor Arce 37, Madrid 28002, Spain.
E-mail: herreras@cajal.csic.es
This work was supported by grants from the Ministerio de Educación y Ciencia, BFU2007-66621/BFI (to OH), BFU2008-04084/BMC (to JS), Comunidad de Madrid, S-SEM-0255-2006 OLFACTOSENSE (to OH), S-GEN-0269-2006 MITOLAB-CM (to JS), Fundación Médica Mutua Madrileña (to BP), and by an institutional grant from the Fundación Ramón Areces to the CBMSO. CIBERER is an initiative of the ISCIII.
Received 19 May 2011; revised 12 August 2011; accepted 15 August 2011; published online 21 September 2011

when many functions are going through a refinement process and in many cases are differently handled as in the adult. Aralar deficiency leads to a loss of respiration on malate plus glutamate, a shutdown of the malate-aspartate NADH shuttle, and in alterations in neuronal aspartate levels and pyruvate to lactate ratios (Jalil *et al*, 2005; Pardo *et al*, 2011) Globally, the aralar-deficient brain shows hypomyelination and a drop of *N*-acetylaspartate and a progressive failure to synthesize glutamine, suggesting that glutamatergic neurotransmission may be compromised in the older animals (Pardo *et al*, 2011). However, the functional state of neurons and circuits in these animals is still unknown. Aralar-knockout (KO) mice show motor deficits, tremor, seizures, and premature death (Jalil *et al*, 2005). A patient with an homozygous loss of function mutation in the gene encoding AGC1 has also low *N*-acetylaspartate levels, hypomyelination, arrested psychomotor development, hypotonia, and seizures (Wibom *et al*, 2009). We here performed an exploration of the electrical activity in postnatal (P15 to P22) mice to gain insight in the functional state and local field potential (LFP) development of the cortex and hippocampus in this early-onset brain disease.

There is little information on postnatal LFP development in mice (Wong *et al*, 2005). Most studies have been made in the rat. Some electrographic events and LFP frequency bands appear already during the first postnatal week (Lahtinen *et al*, 2002), while a transient period of hyperexcitability occurs during the second week. In parallel, a number of cellular and anatomical outbreaks take place, such as axonal reorganization (Gomez-Di Cesare *et al*, 1997), and peaks of expression of connexins and glutamate receptors (Rozental *et al*, 2000; Ritter *et al*, 2002). On the contrary, GABAergic inhibition remains immature. In general, cellular, synaptic, and network electrical properties progress rapidly to stabilize gradually within 1 to 2 months (Kriegstein *et al*, 1987; Huguenard *et al*, 1988). The exploration performed here in the anesthetized Aralar-deficient mice using linear multisite probes to record different types of electrical activity, as LFPs, evoked field potentials, and spontaneous firing rate of single neurons, indicates major deficit in cellular and network electrical activity compatible with progressive behavioral quiescence and status epilepticus in the period P14 to P22. While severely reduced network activity may influence negatively in the activity-dependent circuit refinement, the timeline of wild-type (WT)–KO differences indicate that deficiency in aralar initiates pathology at a very early stage.

Materials and methods

All the experiments were performed in accordance with the European Union guidelines (86/609/EU) and Spanish regulations (BOE 67/8509-12, 1988) regarding the use of laboratory animals. The experimental protocols were approved by the Animal Welfare Committee at the Cajal Institute.

Preparation and Recording

We used mice of both sex deficient for Aralar/AGC1 (Aralar$^{-/-}$) and age-matched WT (*Aralar*$^{+/+}$) littermates from heterozygous breeding pairs (SVJ129 × C57BL6). The generation of Aralar-deficient mice, obtained from Lexicon Pharmaceuticals, Inc. (The Woodlands, TX, USA), and the polymerase chain reaction analysis of genotypes have been described in detail (Jalil *et al*, 2005). Animals were bred in the animal house of the Centro de Biología Molecular (Universidad Autónoma de Madrid) and transported to the Cajal Institute (CSIC, Madrid) for electrophysiological study. Most of the aralar (−/−) mice die at around 23 days. At the end of the period studied P20 to P22, a progressive decline in overall exploratory behavior is observed. Tremor appeared regularly after P19 and tonic-clonic motor seizures were increasingly observed within the 2 to 3 days before animals died. The progression of decline was, however, highly variable among individuals and death time was rather unpredictable. Aralar-KO mice gained no weight within the period P15 to P22 (5 ± 0.2 g; mean ± s.e.m., $n = 20$), while littermates did gain (8.2 ± 0.6 at P15 and 12.1 ± 0.3 at P22; population average: 11.1 ± 0.5 g, $n = 22$).

Mice were anesthetized with a mixture of ketamine (Ketolar 100 mg/kg, intraperitoneally) and xylacine (Rompun, Bayer, 5 mg/kg, intraperitoneally) and placed in a Cunningham-type mouse stereotaxic adaptor (Stoelting Co., Wood Dale, IL, USA). Supplemental doses (1/4 of the initial dosage) were administered every 45 to 60 minutes. The body temperature was maintained at 36°C by a heating element implemented on the adaptor. The stability of the animal was assessed by monitoring the heart rate. Experiments were limited to 4 hours. In general, KO mice showed a notable lability to anesthesia, especially during induction in individuals older than P19. This fact and the variable progression of Aralar-KO mice complicated the customization of groups of age (the study extended over a period of 18 months). Thus, the different types of electrical activities could not be studied on each animal. Except when indicated, at least three animals (normally 5 to 6) were employed for each quantified parameter. Elder KO animals (P20 to P23) presented a high dispersion in behavioral capability, from normally responsive to external stimuli to nearly complete quiescence.

For the reasons outlined, it was not possible to use a standard set of stereotaxic coordinates, making the exploration of hippocampal activity by evoked field potentials arduous and hardly standardizable. We thus limited their use to the best-known and most repeatable ipsilateral CA3–CA1 pathway (Schaffer collateral input). Concentric bipolar stimulating electrodes were placed in the ipsilateral CA3 field for orthodromic activation of the CA1 field. This point was approached at a 30° angle in the sagittal plane. Stimuli (0.1 ms square pulses, 0.1 to 0.8 mA) were applied to elicit the characteristic CA1-evoked potentials (Herreras, 1990). We first used glass micropipettes

)8

(1 to 4 MΩ) filled with 150 mmol/L NaCl. After stimulus site optimization, the glass pipettes were removed and linear multisite silicon probes (Neuronexus, Ann Arbor, MI, USA, A1x16-3mm50-413 and A1x16-5mm100-413) were lowered and connected to a multiple high-impedance headstage. A silver chloride wire in the neck skin served as reference for recording. The signals were amplified and acquired using low noise MultiChannel System recording hardware and software. In a few animals, at the end of the experiment, a small current (10 μA, 3 minutes) was injected through one site of the probe that served for histological verification of recording tracks.

Each animal was recorded with the linear probe in at least three consecutive placements along a single vertical track passing through the cortex, CA1, and CA3/Fascia Dentata (FD) regions in a way that electrode sites laid parallel to the main axis of principal pyramidal and granule cells. Each station aimed to span one of these subregions and covered 750 or 1,500 μm (for 50 and 100 site separation, respectively). Three epochs 3 minutes long were recorded at each station (0.1 Hz to 5 kHz bandpass) and acquired (1 kHz acquisition rate) to a computer. In a selected group of animals, the acquisition rate was increased to 20 kHz to obtain multiunit spike activity after off-line filtering (0.3 to 3 kHz). To minimize the effects of variable anesthetic plane on LFPs, all recordings were made between 10 and 35 minutes after one dose had been delivered. The energy of LFP epochs was estimated on raw signals as well as on its component frequency bands obtained by selective filtering: delta (δ), <2 Hz; theta (θ), 4 to 8 Hz; alpha (α), 10 to 12 Hz; beta (β), 13 to 30; gamma (γ), 30 to 80 Hz. As a gross measurement of the global population synaptic activity, we estimated the average energy of LFP signals (squared voltage) over identical epochs. First, we quantified the LFP power of signals recorded against a far reference electrode in three sites along the same track for each subregion, and the result was averaged. To minimize the effects of volume propagation from subregions producing large LFPs, we repeated the estimation over the same signals in differentiated cortical records (i.e., true LFP) between two consecutive sites separated vertically by 100 μm.

Quantification of Epileptiform Activity

Because of the progressive nature and varying amplitude and waveform of epileptiform activity, the classification and standardization of epileptic events was unfeasible. Thus, we only estimated the frequency of events and explored the underlying currents by current source density (CSD) analysis. The earliest visible epileptiform events (see below) were counted when they extended over at least 150 ms and contained spike activity of amplitude twofold or greater than baseline. At a later stage, epileptiform bouts were easily recognized. Three epochs 1 minute each separated by 4 minutes were quantified on selected electrodes for each animal and pooled together for statistics. To assess whether burst were local or propagated from nearby regions, we applied CSD to interictal-like spikes in the different regions and counted them as local or remote when the field burst presented or not associated current activity.

Unitary Analysis

We aimed to establish a gross relation of average LFP and global spike activity. This was quantified only in the CA1 region whose limits are reliably identified using the evoked potential profiles. Spike activity was estimated on each of the electrode sites spanning the different CA1 layers. No attempt was made to sort units or to identify principal (pyramidal) or putative interneurons. Thus multiunit activity was estimated. Yet, in the CA1 region, cells recorded in layers other than the pyramidal layer can be safely ascribed to putative interneurons (occasional spikes recorded simultaneously in this and an adjacent site were rare and therefore introduced a negligible error). Spikes were counted on filtered (100 Hz to 5 kHz) signals using a voltage threshold of 150 μV ($\sim$2 to 4 times the baseline noise). A grand total of CA1 spike activity was estimated for each animal throughout all recording sites in a single epoch of 180 seconds.

Current Source Density of Evoked and Local Field Potentials

Current source density analysis of LFP profiles provides the magnitude and fine location of the net transmembrane current generated by neural elements contained within a small volume of tissue, eliminating the volume contribution of far sources inherent to LFPs. We employed here the standard unidimensional CSD approach (Herreras, 1990) by estimating the second spatial derivative over the raw LFP profiles. Although there is a notable heterogeneity of tissue resistivity in the Z axis at the level of the stratum pyramidal in mature adult brain (López-Aguado *et al*, 2001), we do not know the precise values of resistivity in immature brain that has much larger volume fraction (Lehmenkühler *et al*, 1993). Therefore, CSD values are expressed in arbitrary units. Admittedly, the unidimensional approach may produce considerable amount of spurious current when applied to raw LFPs due to mutual spatial cancellation among different LFP generators (Korovaichuk *et al*, 2010) or because of the reduced spatial extension of spontaneous synaptic activity that might not meet the criterion of homogeneous activation in the XZ plane. Thus, we only consider reliable the CSD results estimated for specific LFP events whose homogeneity in this plane is known to be at least twofold the interelectrode distance (i.e., 100 μm), such as the epileptic events found in Aralar$^{-/-}$ mice.

Measurement of Cellular Oxygen Consumption

Oxygen consumption rate was measured using a Seahorse XF24 Extracellular Flux Analyzer (Boston, MA, USA) (Qian and Van Houten, 2010). Cortical primary neuronal cultures from P16 Aralar WT and Aralar KO embryos were plated in XF24 V7 cell culture plates (Seahorse Bioscience, North Billerica, MA, USA) at 1.0×10^5 cells/well and incubated for 10 days in a 37°C, 5% CO_2 incubator. The

cell cultures contained >85% of neurons. Cells were equilibrated with bicarbonate-free low-buffered DMEM medium supplemented with 15 mmol/L glucose for 1 hour immediately before XF assay. Substrates were prepared in the same medium and were injected from the reagent ports automatically to the wells at the times indicated. Mitochondrial function in neurons was determined through sequential addition of 6.0 μmol/L oligomycin, 0.5 mmol/L 2,4-dinitrophenol, and 1.0 μmol/L antimycin/1.0 μmol/L rotenone. This allowed determination of basal oxygen consumption, oxygen consumption linked to ATP synthesis, non-ATP linked oxygen consumption (proton leak), uncoupled respiration, and nonmitochondrial oxygen consumption (Qian and Van Houten, 2010).

Western Blotting

Aliquots (50 μg of protein) of hippocampal tissue from 18-day-old Aralar WT and KO mice were homogenated in protease inhibitor cocktail tablet (complete Mini, EDTA-free, Roche, Indianapolis, IN, USA) and sonicated. The homogenate was used for protein determination by the Bradford protein assay and for electrophoretical separation. Samples were electrophoresed in an 8% sodium dodecyl sulfate acrylamide gel and transferred electrophoretically to nitrocellulose membranes, which were blocked in 5% (w/v) dry skimmed milk (Sveltesse, Nestle, Barcelona, Spain) in Tris-buffered saline for 2 hours, and further incubated with antibodies against glutamic-acid-decarboxilase (GAD)-65 (Chemicon polyclonal antibody, 1:1,000, Madrid, Spain) O/N and β-actin (Sigma monoclonal antibody, 1:5,000, Madrid, Spain) for 1 hour at room temperature (RT). Signal detection was performed with and enhanced chemiluminescence substrate (Western lighting-ECL; Perkin-Elmer, Waltham, MA, USA).

Histology

Animals were anesthetized by chloral hydrate (0.5 mg/g body weight; Sigma) and perfused transcardially with saline and formaldehyde (4%). The brains were removed, fixed overnight, and transferred into sucrose. Later, they were embedded in OCT (Tissue-Tek, Sakura Finetek Europe B.V., Zoeterwoude, The Netherlands), and cut (30 μmol/L coronal sections) with a cryotome. Sections were kept in cryoprotectant medium and stored (−20°C) until processing. Sections were stained with cresyl violet and examined with the light microscope.

Statistics

Data are expressed as mean ± standard error of the mean (s.e.m.). Statistical analysis was performed using GraphPad Prism 5.0 software (La Jolla, CA, USA). For investigating the effect of more than one variable within each animal group, we used one-way analysis of variance (ANOVA) followed by the Bonferroni's *post hoc* test. For studying the effect of genotype on one variable, we used the Mann–Whitney test. The effect of genotype on more than one variable was assessed by two-way ANOVA followed by the Bonferroni's *post hoc* test. The significant level (α) was set at 0.05 for each statistical test.

Results

Lack of Local Field Potential Development in Aralar-Knockout Mice

Recording tracks were made through the visual (V2MM) and somatosensory cortices (S1Tr) down to the hippocampus. Under ketamine/xylacine anesthesia, the LFPs were irregular although periodic multiform activity was also present. In all animal groups, the overall LFP activity was larger in the CA3/FD region and smaller in the cortex. Figure 1A shows sample recordings of spontaneous LFP activity in young WT and KO mice at P22 along a track centered in the hilus of the FD. It can be appreciated a notable difference in the baseline amplitude that

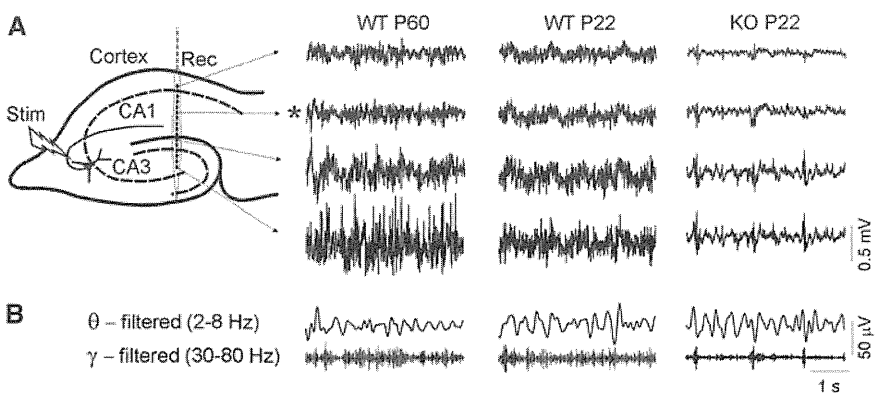

Figure 1 Deficient development of local field potentials (LFPs) in Aralar (−/−) knockout (KO) mice. (**A**) A scheme of electrode placement is illustrated in the scheme. A multielectrode linear probe (Rec) recorded spatial maps of LFPs from the cortex and/or hippocampus. The stimulating electrode (Stim) was placed in the ipsilateral CA3. Sample tracings of LFPs recorded at equivalent sites through hippocampal subfields are shown to the right. Note the reduced amplitude and baseline of LFPs in KO mice as compared with a littermate wild-type (WT) at P22. This in turn is smaller that WT adults (WT 60 days). In all cases, LFPs are greater in the CA3/Fascia Dentata (FD) hippocampal subfield and smallest in the overlying somatosensory cortex. (**B**) Same LFP segments filtered in two different frequency bands (θ and γ) as recorded in the CA1 st. radiatum (asterisk in **A**).

was smallest in KO mice. At this age, LFPs in WT specimens had not reached the final power of adults (compared with sample recordings in WT P60). The power of ongoing LFPs was estimated in three gross regions along the same vertical track, the neocortex, and the CA1 and CA3/FD subregions of the hippocampus, each quantified as an average of three separated locations. We also searched for possible frequency-specific bands (see sample filtered traces in Figure 1B).

Multiple comparisons yielded the following main observations. The LFP power was higher in CA3/FD and lowest in the cortex in all animal groups (Figure 2A; one-way ANOVA, $P<0.0001$ for all groups). Local field potential analysis (two-way ANOVA) between young (P15 to P23) and adult WT (>P60) specimens revealed that the LFP power was age and region-dependent, showing a strong age-by-region interaction ($F_{2,27}=6.38$, $P=0.005$; Figure 2A). Bonferroni's *post hoc* test showed that during development, the LFP power is significantly lower in the CA3/FD region (***$P<0.001$; Figure 2A).

Knockout mice showed much weaker LFPs than WT specimens of the same age (Figure 2A, gray versus white bars). A significant genotype effect was observed (two-way ANOVA; $F_{1,36}=48.32$, $P<0.0001$), with Aralar$^{-/-}$ mice showing lower LFP power in all the analyzed regions (cortex and CA1: ***$P<0.001$; CA3/FD: *$P<0.05$, Bonferroni's *post hoc* test).

Then, we analyzed possible changes on each of the LFP frequency bands (see Materials and methods). Some peculiarities were observed (Figure 2B). In the cortex and CA1 regions, the lowest LFP frequencies (δ) augmented proportionally stronger in WT specimens, while higher frequencies (β and γ) did it in the CA3/FD region at the expense of a decrease in δ and θ content. As it concerns to KO animals, while the absolute LFP power was smaller in all frequency bands compared with WT littermates (not shown), we did not observe any significant difference in the percentage of relative power at any specific band (two-way ANOVA; Figure 2B). However, when comparing the Aralar$^{-/-}$ mice versus the adult WT, we observed a decrease in the γ frequency in CA1 and an increase in the θ content in the CA3/FD region (γ: *$P<0.05$; θ: **$P<0.01$; Figures 1B and 2B; two-way ANOVA, Bonferroni's *post hoc* test).

Since we found a gradation of the LFP power that increased from the cortex toward CA1 and CA3/FD regions, we explored the possibility that the estimations in cortical LFPs reflected changes in far stronger generators due to volume propagation. True local fields were thus estimated in differentiated recordings between pairs of electrodes (see Materials and methods). The analysis confirmed that cortical LFP activity was indeed weaker in KO as compared with WT littermates, albeit in a smaller degree than estimated with ground-referenced recordings (WT/KO mean power ratio was 1.74 and 3.58, respectively; compare white and gray bars in Figures 2C and 2A, CX).

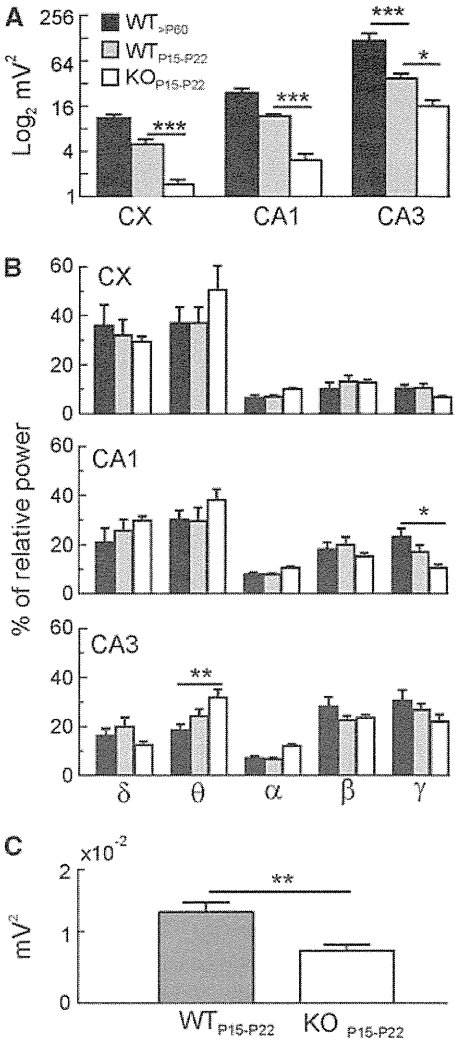

Figure 2 Comparison of local field potentials (LFPs) in wild-type (WT) and knockout (KO) mice. (**A**) Estimation of absolute power of LFPs in different regions (data pooled by groups). To facilitate visual comparison, the *Y* axis is in logarithmic (base 2) scale. For each animal group, the amplitude was larger in CA3/Fascia Dentata > CA1 > cortex. (**B**) Decomposition of LFPs in different frequency bands. The frequency content was generally the same in Aralar-KO mice and WT young and adult (only two significant differences were found). Slower frequencies dominated in cortex, while faster frequencies increased toward the CA3. Panels **A** and **B** correspond to ground-referenced recordings. (**C**) In the cortex, the LFP power between closely adjacent recordings was analyzed in younger animals to discern true local activity from remote changes. In this analysis, the cortex also showed smaller LFPs in KO mice, albeit in smaller proportion. (**A–C**) Data represent the mean ± s.e.m. ($n=5$ to 8 animals per group). *$P<0.05$; **$P<0.01$; ***$P<0.001$.

The evolution of raw LFP power from P15 to P22 is shown in Figure 3. An increase was found in all regions, much more pronounced in WT animals. Two-way ANOVA analysis, followed by Bonferroni's *post hoc* test, showed a genotype effect in the evolution for cortex and CA1 regions (cortex: $F_{1,10}=31.9$, ***$P=0.0002$; CA1: $F_{1,18}=2.9$, ***$P<0.0001$), but not

significant genotype-by-day interaction. Surprisingly, a striking reduction of power was found in P20 to P22 WT individuals in the CA3/FD region, which was not analyzed any further. A significant genotype-by-day interaction between WT and Aralar$^{-/-}$ mice (two-way analysis, $F_{6,18}=3.4$, $^{*}P=0.02$) was found, with a maximum difference between animals at P18 ($^{***}P<0.0001$, Bonferroni's *post hoc* test) followed by a steep decay in the LFPs power, much more pronounced in the WT mice.

Reduced Multiunit Activity in the Aralar-Deficient Hippocampal CA1

We next explored the mechanisms of reduced LFP power in Aralar-deficient mice. Most LFP activity in the hippocampus is likely of an inhibitory synaptic nature (Korovaichuk *et al*, 2010), and Aralar is conspicuously present in hippocampal interneurons in the hilus and CA1 region (Berkich *et al*, 2007, and results not shown), which are mainly GABAergic (Somogyi and Klausberger, 2005). Since hippocampal interneurons are often enriched in cytochrome oxidase, in a way that may correlate with their reported rates of spontaneous firing (Kageyama and Wong-Riley, 1982), we quantified the spontaneous firing rate of putative interneurons in the CA1 region. To emphasize possible age-related differences, only two age groups (P16 to P17 and P20 to P21) were employed. The spikes from all units recorded in eight sites along a recording track spanning from the alveus through the st. lacunosum-moleculare were pooled together. Most spike activity was found in dendritic layers (Figure 4). Multiunit activity in WT animals was similar in the two age groups (152 ± 13 and 150 ± 28 spikes/min; n.s., $P>0.1$), while it was much lower in Aralar-KO

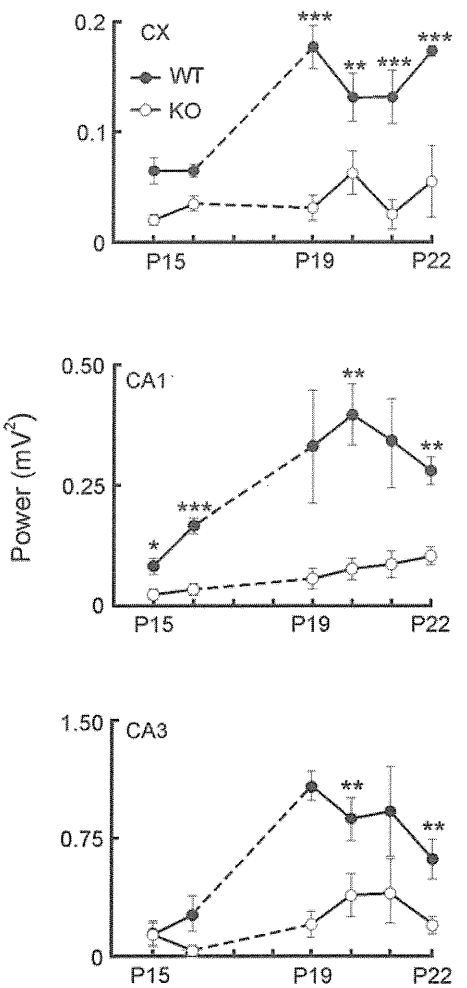

Figure 3 Temporal evolution of local field potential (LFP) power in young wild-type (WT) (filled circles) and knockout (KO) animals (open circles). A gradual increase of LFP power is appreciated in WT animals in all regions, while it was much smaller in KO mice. In all graphs, data represent the mean ± s.e.m. of LFP power at different days. Per area (cortex–CA1–CA3), there are at least three animals per day and group. One-way analysis of variance (ANOVA) (followed by Bonferroni's *post hoc* analysis). $^{*}P<0.05$; $^{**}P<0.01$; $^{***}P<0.001$.

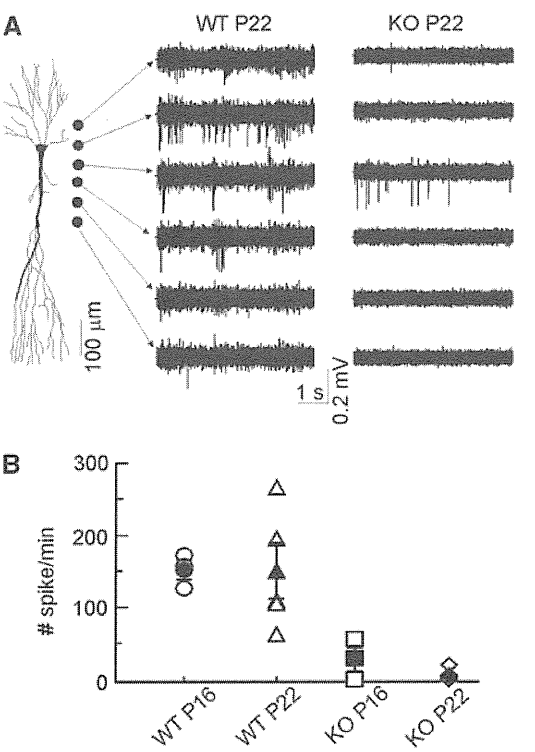

Figure 4 Unitary activity in the CA1 hippocampal subfield. Unitary activity was counted throughout CA1 hippocampal layers. (**A**) Sample tracings filtered to disclose spike activity recorded simultaneously in several locations. Nearly all spikes belong to nonpyramidal cells. A CA1 pyramidal cell is drawn to the left for spatial reference. Knockout (KO) animals displayed a dramatic reduction in spontaneous firing. (**B**) Average CA1 spike activity was estimated as a grand total by pooling spike activity from all units along the CA1 recording sites. There is no difference by age (P16 to 17 *versus* P20 to P21) in wild-type (WT) or KO, but WT had a stronger spike activity than KO in both groups. Data represent mean ± s.e.m ($n=3$ to 5 animals per group).

animals whose CA1 seemed nearly silent, especially at P20 to P21 days (27.7 ± 16 and 4.5 ± 3.2 spikes/min, respectively; Figure 4).

Altered Electrogenesis in the CA1

The synaptic and spike electrogenesis of individual neurons was studied in the CA1 pyramidal population by CSD of the CA3-evoked field potential profiles. Adult animals showed consistent CSD spatiotemporal profiles upon supramaximal stimuli (Figure 5A). The synaptic (CA3-evoked) sink of current (*sk1* in Figure 5) lasted 15 to 20 milliseconds and was centered in the mid stratum radiatum (sample fEPSP marked by two arrows in Figure 5A), surrounded by passive sources in strata pyramidale and lacunosum-moleculare (*sc1* and *sc2* in Figure 5, respectively). This sink was interrupted by a stronger and shorter sink (*sk2*) corresponding to dendro-somatic action currents, that is, those originating the PS (population spike; single arrow in Figure 5A). These originated in the apical shafts ~100 μm below the cell body layer and propagated forwardly to the soma/axon region (curved arrow in Figure 5A). Immediately following the spike sink, a distinct slow passive sink developed in the st. oriens (*sk3*) that indicated the presence of somatic and perisomatic active sources corresponding to recurrent inhibition mediated by basket cells (these overlapped to the passive sources from excitatory synapses in the st. radiatum, i.e., *sc1*). This spatiotemporal profile is essentially the same as in the adult rat (Herreras, 1990). Younger animals showed less consistent CSD maps, in part due to technical difficulties (see Materials and methods) but also to rapidly changing electrogenesis at this period of development. However, a few qualitative differences were consistent enough to be pointed out. Strikingly, the synaptic sink was significantly stronger in Aralar than WT littermates (−2.2 ± 0.1 *versus* −0.9 ± 0.3 mV/mm^2 at P16 to P17 and −2 ± 0.3 *versus* −0.9 ± 0.1 at P20 to P22, respectively). A nonsignificant increase occurred with age in WT animals, while a decrease was appreciated in the KO.

Wild-type animals showed a well-shaped somatic PS at P16 (4.6 ± 0.6 mV; range: 3.4 to 5.4; $n=4$), while it was highly variable in KO animals (5.3 ± 2.3 mV; range: 0 to 11; $n=6$). At P20 to P22, the PS had increased larger in WT (8.2 ± 1.9 mV) than in Aralar-KO mice (6.4 ± 0.7 mV). Population spike amplitude, however, was less reliable (see below) than the spatiotemporal CSD maps that provide the origin and direction of propagation of action currents along the somatodendritic axis. The spike currents in P16 to P17 of WT specimens were initiated in the soma layer and back-propagated into the apical dendrites for ~100 μm (Figure 5B). On the contrary, younger KO animals showed a small current sink (curved arrow in Figure 5C) fanning out from the upper border of the main Schaffer collateral synaptic sink

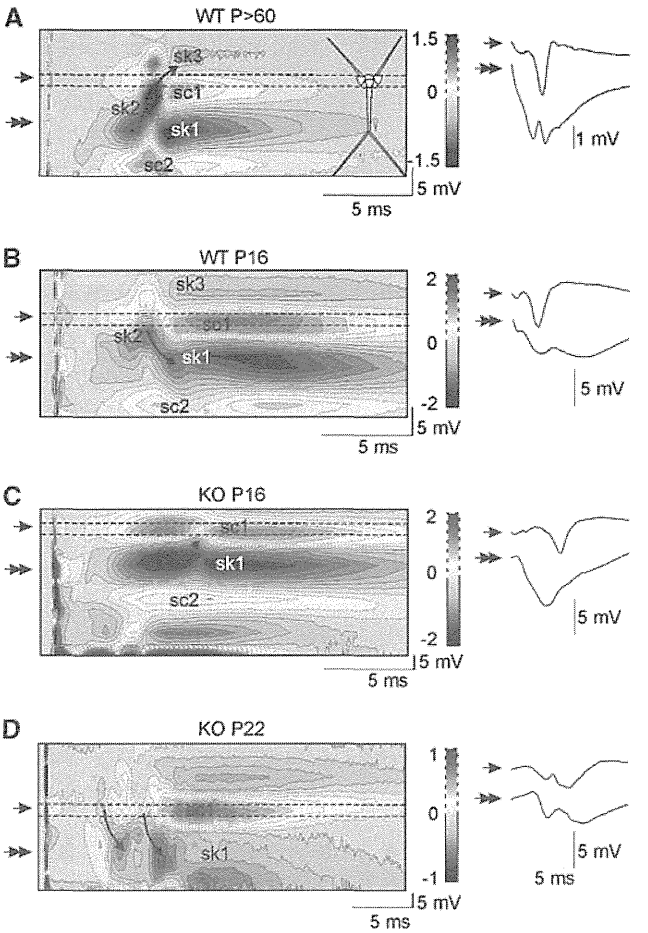

Figure 5 The spike electrogenesis in the CA1 pyramidal population becomes aberrant in knockout (KO) mice. Current source density (CSD) analysis of CA3-evoked field potential maps was employed to unveil the origin and direction of action potential currents. Sample evoked field potentials recorded at the cell body layer and the st. radiatum (single and double arrow, respectively) are to the right of CSD color-coded contour maps. Sinks and sources of current are depicted in blue and yellow/red tones, respectively. (**A**) Standard CSD map in adult wild-type (WT) mice shows apically initiated spike currents propagating toward the soma/axon (see text for full description of synaptic currents). (**B**) At P16, control (WT) mice initiated spike currents in the soma that back-propagated into the apical dendritic tree (curved arrow). (**C**) A representative P16 KO mouse showed weak dendritically initiated spike currents that failed to propagate to the soma/axon region. (**D**) A P22 KO mouse showing aberrant spike multiple currents initiated in the apical shaft and propagating distally. The color reproduction of this figure is available on the *Journal of Cerebral Blood Flow and Metabolism* journal online.

that indicated mild dendritic spike currents propagating forwardly and inconsistently to the soma (i.e., they failed to invade the soma/axon). At P20 to P22, the origin of spike currents in WT animals shifted to adult-like locations within the apical dendrites and propagated both somatically and distally, indicating stronger dendritic spike electrogenesis. Meanwhile, KO animals were highly variable. Some ($n=3$) strikingly presented a similar CSD map as WT

specimens, while others ($n=4$) displayed strongly altered somatodendritic spike sinks of current (see an example in Figure 5), with one or two dendritically initiated small sinks propagating variably and mostly distally.

Progressive Development of Status Epilepticus

In parallel to the above-described changes in LFPs, multiunit activity, and CSD maps in KO animals, we found a progressive development of spontaneous epileptic activity in all three regions examined, cortex, CA1, and CA3. The earliest anomalous activity appeared as bouts of fast γ-like activity lasting $\sim$100 to 150 milliseconds, and had amplitude slightly larger than ongoing LFPs at P16 to P17 (see Figure 6). Such activity evolved in latter days to become a full-blown interictal-like pattern. Notably, interictal spikes were multiform and their amplitude and complexity increased with age (Figure 6). The frequency of events was significantly higher in CA3/FD and lowest in the cortex (cortex: 8 ± 3; CA1: 34 ± 13; CA3/FD: 73 ± 15 events/min, $^{**}P<0.01$, one-way ANOVA followed by Bonferroni's *post hoc* test; $n=8$, P18 to P22; Figure 6C, 1). However, within each region, the rate of events did not significantly change from P18 to P22 (Figure 6C, 2, two-way ANOVA).

We here also suspected a strong volume contribution of epileptic spikes in the CA3/FD region toward distant regions (note the much reduced amplitude in pairs of simultaneous recordings in Figure 6). We therefore performed a detailed exploration using CSD analysis in multiple LFP segments to better localize the source region for epileptic activity. It was found that in all cases, the field epileptic complex begun in the CA3/hilar region. Strikingly, in two out of five animals, these field bursts did not propagate into the CA1, as noted by the absence of currents at the expected times, that is, the local field activity in the CA1 was not generated locally but volume propagated (see example in Figure 6). In epileptic CA3 field spikes examined in five animals, only $16.3\%\pm5.1\%$ propagated to the CA1. The CSD of epileptic bouts in the overlying cortex never showed any local current; hence the small epileptic field bursts were also remote, that is, from the hippocampus.

Bioenergetic Characterization of Intact Aralar-Knockout Cultured Neurons

Basal and coupled oxygen consumption rate in neuronal cultures from Aralar-KO mice were only slightly diminished with respect to those from WT mice (Figure 7). However, the maximal respiration

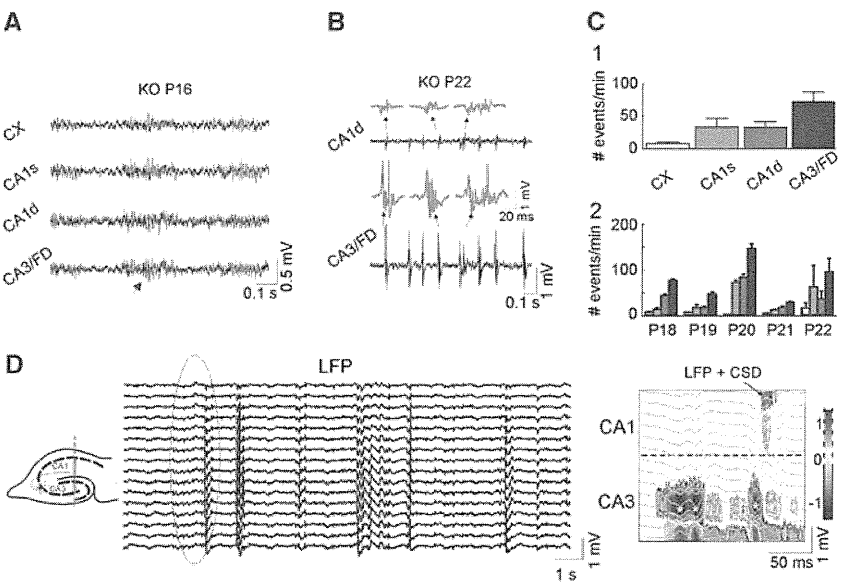

Figure 6 Development of epileptic activity in knockout (KO) animals. (**A**) Sample tracings recorded simultaneously in four locations in a P16 KO. Note periodic bouts of fast activity (arrow) (CA1s and CA1d correspond to somatic and apical dendritic layers, respectively). (**B**) Full interictal field spikes were observed at P22 in KO mice. The sample tracings correspond to the CA1 and CA3/Fascia Dentata (FD) locations. Note the varied form of interictal spikes at the enlarged samples (in gray). (**C**) (1) The rate of epileptic events was higher in the CA3/FD region and smallest in the cortex. Data represent the mean ($\pm$s.e.m.; $n=8$ animals) of the average of five recording traces (1 minute long each) per animal. $^{**}P<0.01$, one-way analysis of variance (ANOVA) followed by Bonferroni's *post hoc* analysis. (2) Although epileptic field events grew larger and complex with age, there was no change in the rate of occurrence. For each day (and area), data represent mean ($\pm$s.e.m.; $n=3$ animals) of the average of five traces (1 minute each) per animal. (**D**) The epileptic field bursts originated always in CA3, but propagated variably to CA1 (16%, see text). A sample tracing of linear local field potential (LFP) recordings in a P21 KO mouse is shown to the left. Recordings span the lower part of the CA1 (from the st. pyramidal) and the CA3/FD region (marked in the scheme in the left). Note multiform epileptic events. A current source density (CSD) contour map of a selected event marked by an oval is shown to the right. Note three large sinks in CA3 (arrows), while only a weak delayed one was generated in CA1 (double arrow).

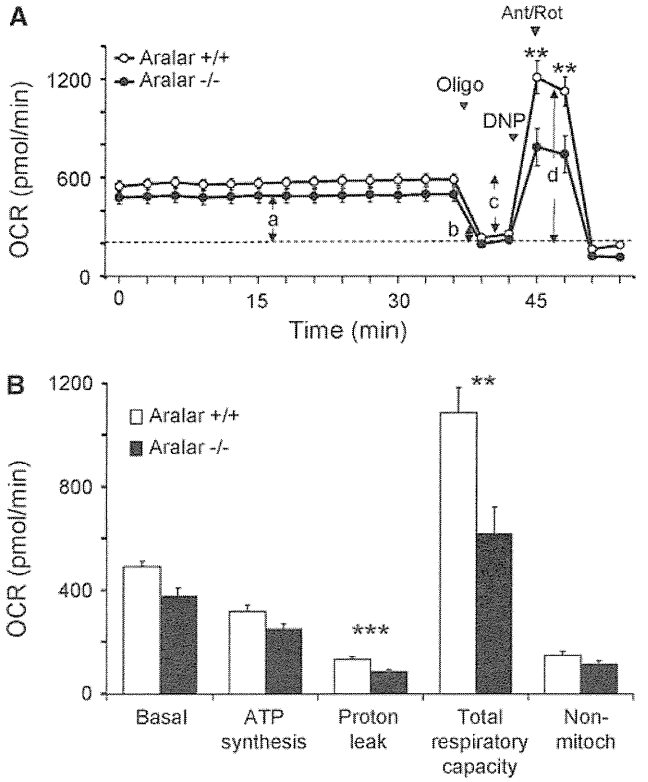

Figure 7 Bionergetic profile in primary neuronal cultures from wild-type (WT) and Aralar-knockout (KO) embryos. (**A**) Oxygen consumption rates (OCRs) in WT and KO neuronal cultures. In all, 6.0 μmol/L oligomycin, 0.5 mmol/L 2,4-dinitrophenol (DNP), and 1.0 μmol/L antimycin/1.0 μmol/L rotenone were injected at times indicated with measurements recorded after injection. The differences in basal mitochondrial respiration (a), proton leak (b), ATP coupled (c), and total respiratory capacity (d) are shown. (**B**) Mitochondrial and nonmitochondrial respiration rates are calculated from (**A**). Mann–Whitney *U*-test. Data are from eight independent experiments (mean ± s.e.m.). $^{**}P < 0.01$; $^{***}P < 0.001$.

obtained in the presence of the uncoupler dinitrophenol is very much reduced in Aralar-deficient neurons. This maximal respiratory activity is limited by the supply of substrates to mitochondria (Brand and Nicholls, 2011), and thus reflects the limitation in glucose-derived pyruvate supply to mitochondria in the absence of a functional malate-aspartate shuttle. This reduced maximal respiratory activity will probably limit ATP production upon neuronal activation and spiking activity of fast firing neurons *in vivo*.

Expression of Glutamic-Acid-Decarboxilase

The gross anatomy was examined in cresyl violet-stained sections (Figure 8A). We did not find noticeable changes in the main architectural features of the cortex and hippocampus in Aralar WT versus KO mice, in agreement with former studies (Jalil *et al*, 2005; Ramos *et al*, 2011). In light of the above results showing the progressive instauration of an epileptic phenotype, we performed a study to determine GAD in the hippocampus (Figure 8B), the enzyme involved in the synthesis of the inhibitory neurotransmitter GABA (γ-aminobutyric acid). The levels of GAD decreased notably in KO animals (ratio of GAD-65/β-actin: 1.5 ± 0.3 WT *versus* 0.8 ± 0.2, $n = 5$; $P < 0.05$, Student's *t*-test) that may result in deficient operation of the inhibitory GABAergic system.

Discussion

The brain uses complementary pathways for energy and metabolite production that may be more or less active throughout the animal's life. Here, we show that genetically modified Aralar-deficient mice

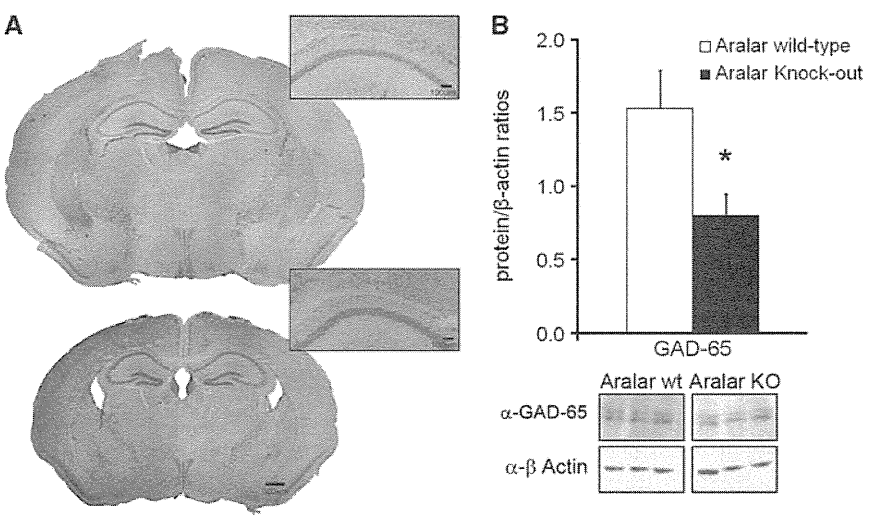

Figure 8 Structural characterization and glutamic-acid-decarboxilase (GAD)-65 quantification in hippocampus from aralar wild-type (WT) and knockout (KO) mice. (**A**) Coronal sections from P18 WT and KO brains were stained with cresyl violet to analyze the structural integrity. (**B**) Western blotting determination of GAD-65 and β-actin proteins in hippocampus from P18 WT and KO brains. ($n = 5$); $^{*}P < 0.05$, Student's '*t*'-test.

lacking mitochondrial NADH malate-aspartate functional shuttle that affects directly to neuroglial metabolic coupling in the brain, develop abnormal electrogenesis in critical postnatal periods that lead to status epilepticus and death. Thus, *Aralar-KO* mice show a poor development of the LFP in cortex and hippocampus in parallel to progressive silencing of spike activity and altered somatodendritic spike electrogenesis. We infer that the reduced synaptic and abnormal spike electrogenesis lie beneath the altered and proto-epileptic phenotype.

Postnatal Electrophysiological Development Is Arrested in Aralar-Knockout Mice

It is known that an important refinement of brain circuits and function takes place after birth. Our electrophysiological monitoring began immediately after weaning, when LFPs have already appeared (Gramsbergen, 1976), and extended through the third postnatal week, since Aralar mice do not survive longer. In this period, LFP growing is drastically slowed down in Aralar-KO mice. An exhaustive interpretation of LFP power is unfeasible as some relevant parameters are unknown, particularly the variable cancellation of mixing sources (Korovaichuk *et al*, 2010). One factor likely having a role during this period is tissue impedance since the extracellular volume fraction reduces from about 45% at birth to 15% to 20% during the first month (Lehmenkühler *et al*, 1993). The end of gliogenesis (Riol *et al*, 1992) plus the continuing arborization of neuron dendrites explain the impedance increase by reduction of the volume fraction. While the gross anatomy of the Aralar-KO mice appears normal (Jalil *et al*, 2005), the delayed development or degeneration of neuronal processes observed in these mice (Ramos *et al*, 2011) and/or altered gliogenesis may be involved. Additional factors appear to be at play. On one side, it is known that Aralar-KO mice are strongly hypomyelinated in central but not peripheral nervous system, most likely because of a shortage of *N*-acetylaspartate, a neuronal precursor of myelin lipids that requires aspartate produced in neurons as a precursor (Jalil *et al*, 2005). Myelination peaks during the third postnatal week in the rat, which may explain the motor and exploratory deficits in Aralar-KO mice 1 to 2 days before death by generalized failure of action potential conduction and sensory-motor integration. Similar phenotypes have been reported in other mutants for myelin components (i.e., the shiverer and jimpy mutants; Honke *et al*, 2002; Saher *et al*, 2005).

We find that hippocampal unitary activity is strongly depressed, even arrested in elder Aralar mice. Although the depression may be overestimated by anesthesia, it explains the reduction in hippocampal LFP power. Thus, most unit activity belongs to putative interneurons recorded outside the pyramidal layer (Ranck, 1973), which in the hippocampus, and possibly the cortex too, are responsible for most of the LFP variance (Korovaichuk *et al*, 2010). The resting Na^+–K^+ ATPase current density in fast spiking interneurons, was found to be three- to sevenfold larger than that of cortical pyramidal neurons, indicating a high energy demand in interneurons (Anderson *et al*, 2010). This is in concordance with the higher number of mitochondria and stronger cytochrome c staining of interneurons compared with principal cells (Gulyás *et al*, 2006). About a dozen different types of interneurons are recognized in the CA1 subfield (Somogyi and Klausberger, 2005) whose activity tailor finely the synaptic integration from afferent nuclei in the projection pyramidal cells. One of LFP frequency bands dominated by interneuron activity is γ oscillation (Bartos *et al*, 2007), which is known to be reduced in several pathophysiological disorders, including epilepsy and ischemia (Barth and Mody, 2011). This frequency band showed a marked reduction in Aralar-KO mice, a result compatible with the reported exquisite dependence of γ oscillations in LFPs on the mitochondrial oxidative capacity (Kann *et al*, 2011).

The very low LFP activity in CA1 in Aralar-KO animals may reflect a limitation in the production of GABA by the interneurons, as indicated by the decreased GAD immunostaining. On the other hand, neurons from Aralar-KO mice have a clear metabolic impairment in glucose utilization due to the lack of a functional malate-aspartate shuttle, which results in an increase in lactate production (Pardo *et al*, 2011). We have now observed that maximal respiration is very much reduced in Aralar-KO neurons, and this will result in a reduced ATP production at the expense of glucose. Therefore, the much reduced LFP activity in CA1 is likely associated with a lack of input from the fast firing interneurons due to failure of these cells to sustain maximal respiration and ATP production in Aralar-KO animals.

On the other hand, although we have not estimated unitary activity of outgoing pyramidal cells, we rarely found spike activity in the cell body layer of Aralar-KO mice. Besides, CSD analysis indicated that KO mice had abnormal spike electrogenesis in these cells in half of the animals tested, consisting on failure of action potential generation in the soma while dendritic action currents are still present (though aberrant too). This may suggest an altered development/localization of Na^+ or other channel types during these critical developmental periods, which may have a role in the final performance of the aralar-KO mouse and perhaps in human AGC1 deficiency (Wibom *et al*, 2009).

We found epileptogenic activity in Aralar-KO mice originating in CA3/hilar region. It may arise from a deficient or delayed maturation of the GABAergic system, which in the rat switches from depolarizing to hyperpolarizing in the second postnatal week (Tyzio *et al*, 2008). In the rat, an early rhythmic bursting activity has been reported in the CA1 that ends by P15

to P16 (Garaschuk *et al*, 1998). An increased propensity to seizure activity has been reported for this period (Mohns *et al*, 2007). The slowed development in Aralar-KO mice may extend the period of natural bursting activity, which may then become pathological (see Le Van Quyen *et al*, 2006).

Alternatively, the epileptic activity may have a different origin. Expectedly, a decreased inhibitory background (silenced interneurons) would render pyramidal cells hyperexcitable. This would not be reflected in evoked or unitary activity in the CA1 region because of the accompanying strong alterations in the intrinsic electrogenesis of pyramidal cells themselves. It was however clearly visible in the CA3 region that undergoes a progressive instauration of status epilepticus. Strikingly, while hypersynchronous activity arises from the CA3, it arrives in an inconsistent manner to the CA1. The frequent failure of CA1 postsynaptic activation by Schaffer collaterals during CA3 bursting activity is unexpected. One possibility is that Schaffer collaterals may drive action potentials inconsistently due to deficient myelination (Jalil *et al*, 2005). In support of this idea, evoked excitatory currents weakened in elder Aralar-KO mice. However, the strongly reduced CA3–CA1–cortex flow of activity does not rule out completely a hippocampal origin for seizure activity in the awaken animal.

We cannot ascertain whether seizures cause the animals death. We never recorded an electrographic seizure under anesthesia. Also, the epileptic activity in the cortex turned out to be volume propagated from the hippocampus. Our speculation is that anesthesia not only depressed ongoing activity, but also raised the threshold for seizure activity. Since the interictal pattern worsened with age in our recordings in anesthetized animals, we may speculate that motor seizures were at some point lethal in awaken animals. Occasionally, we often witnessed a typical motor seizure with tonic-clonic components from which the animal did not recover.

Functional and Clinical Implications

We cannot fix the time point at which electrophysiological abnormalities begin in the Aralar-KO mice since the LFP and evoked field potential differences with control animals were already observed at the earliest postnatal day studied (P15). Postnatal development is a continuum process in which structural (dendritic and axonal arborization and pruning), cellular (receptor and ion channel expression, and insertion in the membranes), and dynamic (activity-dependent synapse stabilization, wiring refinement, activation of silent synapses) factors interact finely (Monyer *et al*, 1994; Bolshakov and Siegelbaum, 1995; Represa and Ben-Ari, 2005; Aizenman and Cline, 2007). Some of these processes evolve in a continuous manner while others have a critical peak in time. Poorly developed early activity in Aralar-KO neurons may thus constitute a negative signal leading to abnormal subcellular progress of the electrogenic mechanisms in neurons, severe decline of neuron spiking, and functional disconnection of circuitry. Astrocytes processes wrap tightly around synaptic neurons and there is increasing evidence for signaling between astrocytes and neurons by way of the release of transmitter molecules such as glutamate (Perea and Araque, 2007). Whether the progressive decline in the synthesis of glutamate and glutamine in astrocytes from Aralar-KO (Pardo *et al*, 2011) is also involved in the abnormal progression of electrogenic mechanisms in aralar-KO neurons is an open question.

Acknowledgements

The authors thank Belén Larrosa for her participation in pilot experiments, and Isabel Manso and Barbara Sesé for technical support. IL-F held a fellowship from the Comunidad de Madrid, Spain.

Disclosure/conflict of interest

The authors declare no conflict of interest.

References

Aizenman CD, Cline HT (2007) Enhanced visual activity *in vivo* forms nascent synapses in the developing retinotectal projection. *J Neurophysiol* 97:2949–57

Anderson TR, Huguenard JR, Prince DA (2010) Differential effects of Na^+–K^+ ATPase blockade on cortical layer V neurons. *J Physiol* 588:4401–14

Barth AM, Mody I (2011) Changes in hippocampal neuronal activity during and after unilateral selective hippocampal ischemia *in vivo*. *J Neurosci* 31:851–60

Bartos M, Vida I, Jonas P (2007) Synaptic mechanisms of synchronized gamma oscillations in inhibitory interneuron networks. *Nat Rev Neurosci* 8:45–56

Berkich DA, Ola MS, Cole J, Sweatt AJ, Hutson SM, LaNoue KF (2007) Mitochondrial transport proteins of the brain. *J Neurosci Res* 85:3367–77

Bolshakov VY, Siegelbaum SA (1995) Regulation of hippocampal transmitter release during development and long-term potentiation. *Science* 269:1730–4

Brand MD, Nicholls DG (2011) Assessing mitochondrial dysfunction in cells. *Biochem J* 435:297–312

del Arco A, Satrústegui J (1998) Molecular cloning of Aralar, a new member of the mitochondrial carrier superfamily that binds calcium and is present in human muscle and brain. *J Biol Chem* 273:23327–34

Garaschuk O, Hanse E, Konnerth A (1998) Developmental profile and synaptic origin of early network oscillations in the CA1 region of rat neonatal hippocampus. *J Physiol (Lond)* 507:219–36

Gomez-Di Cesare CM, Smith KL, Rice FL, Swann JW (1997) Axonal remodeling during postnatal maturation of CA3 hippocampal pyramidal neurons. *J Comp Neurol* 384:165–80

Gramsbergen A (1976) EEG development in normal and undernourished rats. *Brain Res* 105:287–308

Gulyás AI, Buzsáki G, Freund TF, Hirase H (2006) Populations of hippocampal inhibitory neurons express different levels of cytochrome c. *Eur J Neurosci* 23:2581–94

Herreras O (1990) Propagating dendritic action potential mediates synaptic transmission in CA1 pyramidal cells *in situ*. *J Neurophysiol* 64:1429–41

Honke K, Hirahara Y, Dupree J, Suzuki K, Popko B, Fukushima K, Fukushima J, Nagasawa T, Yoshida N, Wada Y, Taniguchi N (2002) Paranodal junction formation and spermatogenesis require sulfoglycolipids. *Proc Natl Acad Sci USA* 99:4227–32

Huguenard JR, Hamill OP, Prince DA (1988) Developmental changes in Na^+ conductances in rat neocortical neurons: appearance of a slowly inactivating component. *J Neurophysiol* 59:778–95

Jalil MA, Begun L, Contreras L, Pardo B, Iijima M, Li MX, Ramos M, Marmol P, Horiuchi M, Shimotsu K, Nakagawa S, Okubo A, Sameshima M, Isashiki Y, del Arco A, Kobayashi K, Satrústegui J, Saheki T (2005) Reduced N-acetylaspartate levels in mice lacking aralar, a brain- and muscle-type mitochondrial aspartate-glutamate carrier. *J Biol Chem* 280:31333–9

Kageyama GH, Wong-Riley MT (1982) Histochemical localization of cytochrome oxidase in the hippocampus: correlation with specific neuronal types and afferent pathways. *Neuroscience* 10:2337–61

Kann O, Huchzermeyer C, Kovács R, Wirtz S, Schuelke M (2011) Gamma oscillations in the hippocampus require high complex I gene expression and strong functional performance of mitochondria. *Brain* 134:345–58

Khazipov R, Luhmann HJ (2006) Early patterns of electrical activity in the developing cerebral cortex of human and rodents. *Trends Neurosci* 29:414–8

Korovaichuk A, Makarova J, Makarov VA, Benito N, Herreras O (2010) minor contribution of principal excitatory pathways to hippocampal LFPs in the anesthetized rat: a combined independent component and current source density study. *J Neurophysiol* 104:484–97

Kriegstein AR, Suppes T, Prince AD (1987) Cellular and synaptic physiology and epileptogenesis of developing rat neocortical neurons *in vitro*. *Dev Brain Res* 431:161–71

Lahtinen H, Palva JM, Sumanen S, Voipio J, Kaila K, Taira T (2002) Postnatal development of rat hippocampal gamma rhythm *in vivo*. *J Neurophysiol* 88:1469–74

Largo C, Cuevas P, Somjen GG, Martin del Río R, Herreras O (1996) The effect of depressing glial function in rat brain *in situ* on ion homeostasis, synaptic transmission, and neuron survival. *J Neurosci* 16:1219–29

Le Van Quyen M, Khalilov I, Ben-Ari Y (2006) The dark side of high-frequency oscillations in the developing brain. *Trends Neurosci* 29:419–27

Lehmenkühler A, Syková E, Svoboda J, Zilles K, Nicholson C (1993) Extracellular space parameters in the rat neocortex and subcortical white matter during postnatal development determined by diffusion analysis. *Neuroscience* 55:339–51

López-Aguado L, Ibarz JM, Herreras O (2001) Activity-dependent changes of tissue resistivity in the CA1 region *in vivo* are layer-specific: modulation of evoked potentials. *Neuroscience* 108:249–62

Mohns EJ, Karlsson KA, Blumberg MS (2007) Developmental emergence of transient and persistent hippocampal events and oscillations and their association with infant seizure susceptibility. *Eur J Neurosci* 26:2719–30

Monyer H, Burnashev N, Laurie DJ, Sakmann B, Seeburg PH (1994) Developmental and regional expression in the rat brain and functional properties of four NMDA receptors. *Neuron* 12:529–40

Pardo B, Rodrigues TB, Contreras L, Garzón M, Llorente-Folch I, Kobayashi K, Saheki T, Cerdán S, Satrústegui J (2011) Brain glutamine synthesis requires neuronal-born aspartate as amino donor for glial glutamate formation. *J Cereb Blood Flow Metab* 31:90–101

Perea G, Araque A (2007) Astrocytes potentiate transmitter release at single hippocampal synapses. *Science* 317:1083–6

Qian W, Van Houten B (2010) Alterations in bioenergetics due to changes in mitochondrial DNA copy number. *Methods* 51:452–7

Ramos M, del Arco A, Pardo B, Martínez-Serrano A, Martínez-Morales JR, Kobayashi K, Yasuda T, Bogónez E, Bovolenta P, Saheki T, Satrústegui J (2003) Developmental changes in the Ca2+-regulated mitochondrial aspartate-glutamate carrier aralar1 in brain and prominent expression in the spinal cord. *Brain Res Dev Brain Res* 143:33–46

Ramos M, Pardo B, Llorente-Folch I, Saheki T, del Arco A, Satrústegui J (2011) The deficiency in the mitochondrial transporter of aspartate/glutamate Aralar/AGC1 causes hypomyelination and neuronal defects unrelated to myelin deficits in mouse brain. *J Neurosci Res*; doi:10.1002/jnr.22639 (e-pub ahead of print)

Ranck Jr JB (1973) Studies on single neurons in dorsal hippocampal formation and septum in unrestained rats. I. Behavioral correlates and firing repertoires. *Exp Neurol* 41:461–531

Represa A, Ben-Ari Y (2005) Trophic actions of GABA on neuronal development. *Trends Neurosci* 28:278–83

Riol H, Fages C, Tardy M (1992) Transcriptional regulation of glial fibrillary acidic protein (GFAP)-mRNA expression during postnatal development of mouse brain. *J Neurosci Res* 32:79–85

Ritter LM, Vazquez DM, Meador-Woodruff JH (2002) Ontogeny of ionotropic glutamate receptor subunit expression in the rat hippocampus. *Dev Brain Res* 139:227–36

Rozental R, Srinivas M, Gokhan S, Urban M, Dermietzel R, Kessler JA, Spray DC, Mehler MF (2000) Temporal expression of neuronal connexins during hippocampal ontogeny. *Brain Res Rev* 32:57–71

Saher G, Brügger B, Lappe-Siefke C, Möbius W, Tozawa R, Wehr MC, Wieland F, Ishibashi S, Nave KA (2005) High cholesterol level is essential for myelin membrane growth. *Nat Neurosci* 8:468–75

Somogyi P, Klausberger T (2005) Defined types of cortical interneurons structure space and spike timing in the hippocampus. *J Physiol (Lond)* 562:9–26

Tyzio R, Minlebaev M, Rheims S, Ivanov A, Jorquera I, Holmes GL, Zilberter Y, Ben-Ari Y, Khazipov R (2008) Postnatal changes in somatic gamma-aminobutyric acid signalling in the rat hippocampus. *Eur J Neurosci* 27:2515–28

Wibom R, Lasorsa FM, Töhönen V, Barbaro M, Sterky FH, Kucinski T, Naess K, Jonsson M, Pierri CL, Palieri F, Wedell A (2009) AGC1 deficiency associated with global cerebral hypomyelination. *N Engl J Med* 361:489–95

Wong T, Zhang XL, Asl MN, Wu CP, Carlen PL, Zhang L (2005) Postnatal development of intrinsic GABAergic rhythms in mouse hippocampus. *Neuroscience* 134:107–20

Xu Y, Ola MS, Berkich DA, Gardner TW, Barber AJ, Palmieri F, Hutson SM, LaNoue KF (2007) Energy sources for glutamate neurotransmission in the retina: absence of the aspartate/glutamate carrier produces reliance on glycolysis in glia. *J Neurochem* 101:120–31

World Journal of Gastroenterology

Online Submissions: http://www.wjgnet.com/esps/
wjg@wjgnet.com
doi:10.3748/wjg.v18.i39.5601

World J Gastroenterol 2012 October 21; 18(39): 5601-5607
ISSN 1007-9327 (print) ISSN 2219-2840 (online)

BRIEF ARTICLE

Biochemical characteristics of neonatal cholestasis induced by citrin deficiency

Jian-She Wang, Xiao-Hong Wang, Ying-Jie Zheng, Hai-Yan Fu, Rui Chen, Yi Lu, Ling-Juan Fang, Takeyori Saheki, Keiko Kobayashi

Jian-She Wang, Department of Pediatrics, Jinshan Hospital, Fudan University, Shanghai 200540, China
Jian-She Wang, Xiao-Hong Wang, Hai-Yan Fu, Rui Chen, Yi Lu, Ling-Juan Fang, The Center for Pediatric Liver Diseases, Children's Hospital of Fudan University, Shanghai 201102, China
Ying-Jie Zheng, Department of Epidemiology, School of Public Health, Fudan University, Shanghai 200032, China
Takeyori Saheki, Institute of Resource Development and Analysis, Kumamoto University, Kumamoto 860-0811, Japan
Keiko Kobayashi, Department of Molecular Metabolism and Biochemical Genetics, Kagoshima University Graduate School of Medical and Dental Sciences, Kagoshima 890-8544, Japan
Author contributions: Wang JS, Wang XH, Zheng YJ and Fu HY contributed equally to this paper; Wang JS proposed the idea and wrote the first draft of this paper; Zheng YJ contributed to the statistical analysis and created all the figures; Fu HY contributed to the data collection; Wang JS, Fu HY, Chen R, Saheki T and Kobayashi K contributed to the gene tests and Western blotting; Wang JS, Wang XH and Lu Y contributed to patient management; and all the authors contributed to the design, data analysis, draft revision and final approval of the paper for publishing.
Supported by National Science Foundation of China, No. 30973230 and No. 81070281
Correspondence to: Jian-She Wang, Professor, Department of Pediatrics, Jinshan Hospital, Fudan University, Shanghai 200540, China. jshwang@shmu.edu.cn
Telephone: +86-21-64931171 Fax: +86-21-64931171
Received: April 12, 2012 Revised: June 27, 2012
Accepted: July 9, 2012
Published online: October 21, 2012

Abstract

AIM: To explore differences in biochemical indices between neonatal intrahepatic cholestasis caused by citrin deficiency (NICCD) and that with other etiologies.

METHODS: Patients under 6 mo of age who were referred for investigation of conjugated hyperbilirubinaemia from June 2003 to December 2010 were eligible for this study. After excluding diseases affecting the extrahepatic biliary system, all patients were screened for the two most common *SLC25A13* mutations; the coding exons of the entire *SLC25A13* gene was sequenced and Western blotting of citrin protein performed in selected cases. Patients in whom homozygous or compound heterozygous *SLC25A13* mutation and/or absence of normal citrin protein was detected were defined as having NICCD. Cases in which no specific etiological factor could be ascertained after a comprehensive conjugated hyperbilirubinaemia work-up were defined as idiopathic neonatal cholestasis (INC). Thirty-two NICCD patients, 250 INC patients, and 39 infants with cholangiography-confirmed biliary atresia (BA) were enrolled. Laboratory values at their first visit were abstracted from medical files and compared.

RESULTS: Compared with BA and INC patients, the NICCD patients had significantly higher levels of total bile acid (TBA) [all measures are expressed as median (inter-quartile range): 178.0 (111.2-236.4) μmol/L in NICCD *vs* 112.0 (84.9-153.9) μmol/L in BA and 103.0 (70.9-135.3) μmol/L in INC, $P = 0.0001$]. The NICCD patients had significantly lower direct bilirubin [D-Bil 59.6 (43.1-90.9) μmol/L in NICCD *vs* 134.0 (115.9-151.2) μmol/L in BA and 87.3 (63.0-123.6) μmol/L in INC, $P = 0.0001$]; alanine aminotransferase [ALT 34.0 (23.0-55.0) U/L in NICCD *vs* 108.0 (62.0-199.0) U/L in BA and 84.5 (46.0-166.0) U/L in INC, $P = 0.0001$]; aspartate aminotransferase [AST 74.0 (53.5-150.0) U/L in NICCD *vs* 153.0 (115.0-239.0) U/L in BA and 130.5 (81.0-223.0) U/L in INC, $P = 0.0006$]; albumin [34.9 (30.7-38.2) g/L in NICCD *vs* 38.4 (36.3-42.2) g/L in BA and 39.9 (37.0-42.3) g/L in INC, $P = 0.0001$]; glucose [3.2 (2.0-4.4) mmol/L in NICCD *vs* 4.1 (3.4-5.1) mmol/L in BA and 4.0 (3.4-4.6) mmol/L in INC, $P = 0.0014$] and total cholesterol [TCH 3.33 (2.97-4.00) mmol/L in NICCD *vs* 4.57 (3.81-5.26) mmol/L in BA and 4.00 (3.24-4.74) mmol/L in INC, $P = 0.0155$] levels. The D-Bil to total bilirubin (T-Bil) ratio was significantly lower in NICCD patients [all measures

are expressed as median (inter-quartile range): 0.54 (0.40-0.74)] than that in BA patients [0.77 (0.72-0.81), P = 0.001] and that in INC patients [0.74 (0.59-0.80), P = 0.0045]. A much higher AST/ALT ratio was found in NICCD patients [2.46 (1.95-3.63)] compared to BA patients [1.38 (0.94-1.97), P = 0.0001] and INC patients [1.48 (1.10-2.26), P = 0.0001]. NICCD patients had significantly higher TBA/D-Bil ratio [3.36 (1.98-4.43) *vs* 0.85 (0.72-1.09) in BA patients and 1.04 (0.92-1.14) in INC patients, P = 0.0001], and TBA/TCH ratio [60.7 (32.4-70.9) *vs* 24.7 (19.8-30.2) in BA patients and 24.2 (21.4-26.9) in INC patients, P = 0.0001] compared to the BA and INC groups.

CONCLUSION: NICCD has significantly different biochemical indices from BA or INC. TBA excretion in NICCD appeared to be more severely disturbed than that of bilirubin and cholesterol.

Key words: Cholestasis; Biliary atresia; Infants; Idiopathic neonatal cholestasis; *SLC25A13*

Peer reviewer: Dr. Stefan Wirth, Professor, Children's Hospital, Heusnerstt. 40, 42349 Wuppertal, Germany

Wang JS, Wang XH, Zheng YJ, Fu HY, Chen R, Lu Y, Fang LJ, Saheki T, Kobayashi K. Biochemical characteristics of neonatal cholestasis induced by citrin deficiency. *World J Gastroenterol* 2012; 18(39): 5601-5607 Available from: URL: http://www.wjgnet.com/1007-9327/full/v18/i39/5601.htm DOI: http://dx.doi.org/10.3748/wjg.v18.i39.5601

INTRODUCTION

Citrin deficiency, caused by mutations in the *SLC25A13* gene on chromosome 7q21.3, is an autosomal recessive disease that was first discovered in Japan and thereafter identified worldwide[1-8]. At least two main phenotypes of citrin deficiency have been established: neonatal intrahepatic cholestasis caused by citrin deficiency (NICCD, OMIM #605814)[9-11] and adult-onset type II citrullinemia (CTLN2, OMIM #603471)[1,12]. The clinical features and diagnostic criteria of CTLN2 have been well established, but those of NICCD have not yet been established.

Children with NICCD usually have transient intrahepatic cholestasis that disappears by the age of 1 year with appropriate management[13]. However, some patients need liver transplantation or may die from the disease during infancy[14-17]. Others may develop severe CTLN2 symptoms unexpectedly one to several decades later[13]. Prompt detection and specific lactose-free and/or medium-chain triglyceride formula may contribute to the avoidance of a complicated course in the NICCD phase. However, the prompt diagnosis of NICCD is still a challenge because the clinical features of cholestasis induced by citrin deficiency are presently not fully understood[18].

Some biochemical indices, including total bilirubin (T-Bil), direct bilirubin (D-Bil), aspartate aminotransferase (AST), alanine aminotransferase (ALT), alkaline phosphatase (ALP), γ-glutamyltranspeptidase (GGT), and α-fetoprotein (AFP) have been analyzed or compared between patients with NICCD, biliary atresia (BA) or idiopathic neonatal cholestasis (INC), with significant differences found between them[4]. However, comparisons of serum total bile acid (TBA) and total cholesterol (TCH) levels between different causes of neonatal cholestasis has rarely been reported before[19].

Bilirubin, bile acids and cholesterol are all mainly physiologically excreted by the hepatobiliary system. Usually, the blood levels of all these compounds increase in the event of blockage of the extrahepatic biliary system. However, they may be affected to different extents in intrahepatic cholestasis with different etiology. For instance, blood TCH and TBA levels are usually elevated significantly in Alagille syndrome, even in cases in which the bilirubin level is only mildly elevated; however, the blood TCH level is usually normal in cases of progressive familial intrahepatic cholestasis type 1 or 2 despite significant elevation of blood TBA and bilirubin levels. Therefore, comparison of these biochemical indices in neonatal cholestasis cases with different etiologies will enable better characterization of the biochemical changes of the disease and may help elucidate the mechanism of cholestasis caused by citrin deficiency.

Therefore, the aims of this study were to explore the differences in biochemical indices, including D-Bil, TBA, TCH and their ratios between cholestasis with different etiologies, and to explore the mechanism of cholestasis caused by citrin deficiency.

MATERIALS AND METHODS

Subjects

Patients under 6 mo of age who were referred to the Children's Hospital of Fudan University, a tertiary referral hospital and primary specialized paediatric hospital in Eastern China, from June 2003 to December 2010, for investigation of conjugated hyperbilirubinaemia were eligible for this study. Conjugated hyperbilirubinemia was defined as serum T-Bil levels > 75 μmol/L, with a conjugated fraction accounting for > 20% of the total, or having conjugated bilirubin levels > 17 μmol/L with serum T-Bil levels < 75 μmol/L[20]. Patients who had obvious extrahepatic abnormalities or prolonged prothrombin time that could not be corrected by parenteral administration of vitamin K1 were excluded. Subjects who satisfied the above criteria as well as the following specific criteria for each of the three groups were included.

BA group: Patients with neonatal cholestasis in whom no isotope excretion was demonstrated by hepatobiliary iminodiacetic acid (HIDA) scintigraphy, and in whom diagnosis of BA was confirmed by laparoscopic or laparotomic cholangiography were eligible for this group.

INC group: Intrahepatic cholestasis was defined as con-

Table 1 Differential diagnosis have been excluded

Affecting bile duct	Infectious	Metabolic	Others
Biliary atresia	Herpes viruses	α-1 antitrypsin deficiency	Endocrinological
Choledochal cyst	Rubella virus	Neonatal iron storage disease	Hypothyroidism
Cholelithiasis	Enteroviruses	Amino acid disorders	Panhypopituitarism/septo-optic dysplasia
Inspissated bile	Hepatitis viruses	Tyrosinemia	Genetic
Tumor	Human immunodeficiency virus	Hypermethioninemia	ATP8B1 deficiency
Hemangioma	Syphilis	Mevalonate kinase dificiency	ABCB11 deficiency
Bile duct stenosis/stricture/perforation	Toxoplasmosis	Glucogen storage diseases	ABCB4 deficiency
Neonatal sclerosing cholangitis	Bacterial sepsis	Gaucher disease	Bile acid synthetic defects
Caroli disease	Urinary tract infections	Niemann-Pick disease	Neonatal Dubin-Johnson syndrome
Alagille syndrome		Wolman disease	Various trisomies
		Zellweger syndrome	Arghrogryposis
		Infantile Refsum disease	Hematological
		Mitochondrial disorders	Hemophagocytic lymphohistiocytosis
		Urea cycle disorders	Langerhans cell histiocytosis
			Miscellaneous drug effects
			Total parenteral nutrition

jugated hyperbilirubinemia following the exclusion of diseases affecting the extrahepatic biliary system (Table 1) by imaging of the hepatobiliary system. The imaging procedures included an ultrasound scan and HIDA scintigraphy in each case and laparotomic/laparoscopic cholangiography in selected cases. Idiopathic neonatal cholestasis (INC) was defined when no specific etiological factor (Table 1) could be ascertained after a comprehensive conjugated hyperbilirubinemia test[21]. Patients with at least single-allele mutation of *SLC25A13* gene were excluded from this group as well.

NICCD group: The strategy of testing for *SLC25A13* gene mutations in intrahepatic cholestatic infants had been reported previously[22,23]. All intrahepatic cholestasis infants with unknown causes were screened for the two most common mutations of the *SLC25A13* gene in Chinese, 851del4 and 1638ins23. For patients with various aminoacidemia or patients with only single-allele mutation who were found by the above screening method, the entire 18 coding exons together with the flanking sequence of the *SLC25A13* gene were amplified by polymerase chain reaction and directly sequenced. Western blotting analysis of citrin protein was performed on patients with biopsied liver specimens available. Only patients in whom homozygous or compound heterozygous *SLC25A13* gene mutation and/or absence of normal citrin protein were demonstrated, for whom a definite diagnosis of citrin deficiency could be made, were regarded as NICCD patients in this study. Patients with a probable diagnosis of citrin deficiency, that is, in whom there was only a heterozygous *SLC25A13* gene mutation and in whom absence of normal citrin protein could not be demonstrated by Western blotting were excluded.

Retrospective analyses of biochemical indices

The medical files of the patients who satisfied the above inclusion and exclusion criteria were reviewed following the approval of the Institute's Ethics Review Committee. Sex, birth weight, gestation age or term/preterm, age at which conjugated jaundice was first noticed, and the biochemical indices at presentation, were abstracted. Liver function tests and other routine laboratory data were obtained using standard methods.

Statistical analysis

Statistical analysis was performed using Stata/SE 10.0 for Windows (StataCorp LP, College Station, TX, United States of America). The descriptive data of the quantitative variables were reported in box-whisker plots and compared using Kruskal-Wallis rank tests among the three groups. For results with overall statistical significance, a Mann-Whitney test with a Bonferroni correction was further performed to test the medians between a series of pairwise groups. All *P* values were two-sided. Results were considered statistically significant at the 0.05 level.

RESULTS

Basic information

In total, 32 patients (19 male and 13 female) with a definite diagnosis of citrin deficiency were included in the NICCD group. Thirty-nine patients (24 male and 15 female) were included in the BA group. Two hundred and fifty patients (174 male and 76 female) were included in the INC group. The birth weight and the days at which conjugated jaundice was first noticed in the three groups are illustrated in Figure 1 or Table 2. The median birth weight was lowest in the NICCD group, but the difference did not reach statistical significance (Table 2). Conjugated jaundice was noticed earlier in the BA group compared with the INC group ($P < 0.05$, Figure 1A).

Comparison of biochemical indices among three groups

The biochemical data of the three groups were compared (Figure 1B-E, Table 2). The NICCD group had significantly lower ALT, AST, total protein, albumin, and glucose levels compared with the BA and INC groups, suggesting that the synthetic function and glucose metabolism were more severely damaged in the NICCD

Table 2 Comparison of birth weight, biochemical indices and their ratios among the three groups

	Reference range and unit	BA (n = 39)		INC (n = 39)		NICCD (n = 32)	
		Median	Inter-quartile	Median	Inter-quartile	Median	Inter-quartile
Birth weight	2.5-4.0 kg	3.2	2.9-3.8	3.1	2.8-3.5	2.9	2.4-3.4
Biochemical indices							
T-Bil[ac]	2-20 mmol/L	159.5	140.2-201.4	133.8	90.0-190.4	112.7	64.4-165.4
D-Bil[ace]	0-6 mmol/L	134	115.9-151.2	87.3	63.0-123.6	59.6	43.1-90.9
ALT[ce]	< 40 IU/L	108	62.0-199.0	84.5	46.0-166.0	34	23.0-55.0
AST[ce]	< 40 IU/L	153	115.0-239.0	130.5	81.0-223.0	74	53.5-150.0
GGT[ac]	< 50 IU/L	558	300.0-1086.0	155	91.0-294.0	187.5	136.0-253.0
TBA[ce]	< 40 mmol/L	112	84.9-153.9	103	70.9-135.3	177.9	111.2-236.4
Total protein[ce]	55-78 g/L	57.4	55.3-63.1	57.2	52.5-62.8	48.5	44.5-53.9
Albumin[ce]	35-55 g/L	38.4	36.3-42.2	39.9	37.0-42.3	34.9	30.7-38.2
Glucose[ce]	3.9-5.9 mmol/L	4.1	3.4-5.1	4	3.4-4.6	3.2	2.0-4.4
TCH[ce]	3.12-5.20 mmol/L	4.57	3.81-5.26	4	3.24-4.74	3.33	2.97-4.00
Ratios							
D-Bil/T-Bil[ace]		0.77	0.72-0.81	0.74	0.59-0.80	0.54	0.40-0.74
AST/ALT[ce]		1.38	0.94-1.97	1.48	1.10-2.66	2.46	1.95-3.63
TBA/D-Bil[ace]		0.85	0.72-1.09	1.04	0.92-1.14	3.36	1.98-4.43
D-Bil/TCH[ac]		30.2	22.8-34.0	21.5	16.7-31.2	18.7	13.9-26.6
TBA/TCH[ce]		24.7	19.8-30.2	24.2	21.4-26.9	60.7	32.4-70.9

[a]P < 0.05 between BA and INC; [c]P < 0.05 between BA and NICCD; [e]P < 0.05 between INC and NICCD. NICCD: Neonatal intrahepatic cholestasis caused by citrin deficiency; BA: Biliary atresia; INC: Idiopathic neonatal cholestasis; TBA: Total bile acid; T-Bil: Total bilirubin; D-Bil: Direct bilirubin; AST: Aspartate aminotransferase; ALT: Alanine aminotransferase; GGT: γ-glutamyltranspeptidase; TCH: Total cholesterol.

group than in the other two groups. The NICCD group also had significantly higher TBA and lower D-Bil and cholesterol levels compared with the BA and INC groups, indicating that the excretion of bile acids, D-Bil and cholesterol might be affected differently in NICCD patients. Significantly lower T-Bil and GGT levels were noticed in the NICCD group only when compared with the BA group.

Comparison of ratios of biochemical indices

To compare further the different biochemical indices, a series of ratios was calculated. The highest ratio of D-Bil to T-Bil was found in the BA group and the lowest in the NICCD group (Table 2, Figure 1F). A much higher AST/ALT ratio was found in the NICCD group compared to the INC and BA groups (Table 2).

The ratios between D-Bil, bile acids and cholesterol were also compared (Table 2). The ratio of serum TBA to D-Bil was significantly higher in the NICCD group than the ratios in the BA and INC groups (Figure 1G, P < 0.05). Significant differences were also found for the ratio of TBA to TCH between the NICCD and BA groups and between the NICCD and INC groups (Figure 1H, P < 0.05).

DISCUSSION

Citrin deficiency is one of the most common classical inborn errors of metabolism of amino acids, organic acids and fatty acid oxidation in Eastern Asia, including China[24]. The biochemical characteristics and mechanism of cholestasis caused by citrin deficiency are still not fully understood. Although differences in some indices among patients with BA, INC and NICCD have been reported previously, the very small sample sizes of the studies precluded a definite conclusion[4,19,23]. In the present study, the cohorts of NICCD, INC and BA had numbers large enough to test previous findings. Additionally, by comparing the elevation of D-Bil, TBA and cholesterol levels and the ratios of these compounds, it was found that the excretion of bile acids appeared to be more severely affected in NICCD than in BA and INC.

A previous study with a small number of subjects demonstrated that patients with cholestasis caused by citrin deficiency had lower ALT and AST levels and higher AST to ALT ratios compared to those with BA or idiopathic neonatal hepatitis[25]. Low albumin and glucose levels were also associated with NICCD in a previous case series[26,27]. In the present study, those findings were confirmed. Previous studies also showed that patients with NICCD had lower birth weight compared to normal controls or to the national standard. In our study, although a lower median birth weight in the NICCD group was noticed, the differences did not reach statistical significance compared to patients with BA or INC. This could be explained by the different control groups (normal control or national standard used in previous studies *vs* patients with cholestasis of other causes) and the large difference observed within the NICCD group in this study.

The serum TBA level in NICCD has previously been compared with that in BA and INC in a study that had very few subjects[19]. In the present study, the serum level of TBA as well as the ratio of serum TBA to D-Bil and cholesterol levels was compared. In BA, we can suppose that excretion of D-Bil, bile acids and cholesterol is affected to the same extent in consideration of complete blockage of the biliary system. If the ratio of TBA to D-Bil in the BA group was taken as the reference value, the median for INC was found to be 1.22 (1.04/0.85) times higher